Pore characteristics of lacustrine shale within the oil window in the Upper Triassic Yanchang Formation, southeastern Ordos Basin, China

Article *in* Marine and Petroleum Geology · January 2018

DOI: 10.1016/j.marpetgeo.2018.01.013

CITATIONS
8

READS
259

9 authors, including:

Huijuan Guo
Chinese Academy of Sciences
4 PUBLICATIONS **78** CITATIONS
SEE PROFILE

Ruliang He
Syracuse University
2 PUBLICATIONS **16** CITATIONS
SEE PROFILE

Wanglu Jia
Chinese Academy of Sciences
25 PUBLICATIONS **217** CITATIONS
SEE PROFILE

Xiaorong Luo
Chinese Academy of Sciences
63 PUBLICATIONS **595** CITATIONS
SEE PROFILE

Marine and Petroleum Geology 91 (2018) 279–296

Contents lists available at ScienceDirect

Marine and Petroleum Geology

journal homepage: www.elsevier.com/locate/marpetgeo

Research paper

Pore characteristics of lacustrine shale within the oil window in the Upper Triassic Yanchang Formation, southeastern Ordos Basin, China

Huijuan Guo[a,b], Ruliang He[a,b], Wanglu Jia[a,*], Ping'an Peng[a], Yuhong Lei[c], Xiaorong Luo[c], Xiangzeng Wang[d], Lixia Zhang[d], Chengfu Jiang[d]

[a] State Key Laboratory of Organic Geochemistry, Guangzhou Institute of Geochemistry, Chinese Academy of Sciences, Guangzhou 510640, China
[b] University of Chinese Academy of Sciences, Beijing 100049, China
[c] Institute of Geology and Geophysics, Chinese Academy of Sciences, Beijing 100029, China
[d] Shaanxi Yanchang Petroleum (Corporation) Company Limited, Xi'an 710075, China

ARTICLE INFO

Keywords:
Pore characteristics
Petroleum expulsion and retention
Extracellular polymeric substances
OM type
Compaction
Mature lacustrine shale
Yanchang Formation

ABSTRACT

Organic matter (OM)-rich shale in the Yanchang Formation is recognized as a promising hybrid shale oil/shale gas system in lacustrine strata in China. Being mainly in the oil window, both the type and distribution of the pores in the shale have been affected by several factors, including petroleum expulsion and retention, mineral and organic composition, and compaction. To obtain a better understanding of the factors controlling OM pore development, 10 core samples were selected with various OM content from the Chang 7 and Chang 9 members of the Yanchang Formation for pore characterization. The investigation combined microscopic observation, both of thin sections and ion milled surfaces of samples with low-pressure carbon dioxide and nitrogen adsorption and bulk porosity measurements, with the main emphasis being on OM-associated pores.

The selected samples generally have relatively low total porosity, with the pores being poorly connected. Most pore types found in marine shales were present. The size of porous OM is usually small, mostly measuring several hundreds of nanometers to a few micrometers, which suggest a general compaction effect on pore development. The pore development is related to different petroleum expulsion processes. Shale with very porous OM was a very important feature. The OM coexisting with fluorescent lipitinites was present in a cross-linked nanofiber structure, possibly related to altered extracellular polymeric substances (EPS) by compaction and maturation. Various OM types that varied in both size and shape did not contain any visible pores (e.g. woody relics, migrated solid bitumen and OM laminae in close association with clay minerals). Unusually low meso- and macropore volume in the sample with the highest total organic carbon (TOC) content was confirmed by the predominance of OM laminae without visible pores; however, abundant micropores were indicated by CO_2 adsorption analysis. Meso- and macropores in this sample had probably not developed due to a significant compaction effect. Due to the small numbers of studied samples, these OM pore characteristics need to be viewed with caution.

1. Introduction

Pores in shale not only provide the space for petroleum storage, but also form the flow-path network for liquids and gases. Therefore, the porosity and distribution characteristics of pores (e.g., their size, type and connectivity) are important for resource potential evaluation and development of unconventional shale reservoirs (Bustin et al., 2008; Loucks et al., 2009; Ross and Bustin, 2009; Schieber, 2010; Sondergeld et al., 2010; Wang and Reed, 2009). Most of the investigated shale units, ranging in age from the Late Proterozoic to the Paleogene, were deposited in marine environments (Chalmers et al., 2012; Fishman et al., 2012; Klaver et al., 2015; Löhr et al., 2015; Loucks et al., 2009, 2012; Lu et al., 2015; Mastalerz et al., 2013; Milliken et al., 2013; Pommer and Milliken, 2015; Ross and Bustin, 2007, 2009; Slatt and O'Brien, 2011; Zeng et al., 2016). However, lacustrine shales have contributed a large proportion of conventional petroleum production in several parts of the world, including China, Africa, Brazil, etc. (Katz, 1990; Katz and Lin, 2014). They may, therefore, have unconventional resource potential. Lacustrine shales differ largely from marine shales due to their limited geographical distributions, their sensitivity to very frequent changes in climate, and the large number of interbedded sand and mud layers (Fang et al., 2016; Katz and Lin, 2014; Ko et al., 2017;

* Corresponding author. Guangzhou Institute of Geochemistry, Chinese Academy of Sciences, 511 Kehua Street, Tianhe District, Guangzhou 510640, China.
E-mail address: wljia@gig.ac.cn (W. Jia).

https://doi.org/10.1016/j.marpetgeo.2018.01.013
Received 17 March 2017; Received in revised form 4 January 2018; Accepted 10 January 2018
Available online 11 January 2018
0264-8172/

Lei et al., 2015; Wang et al., 2016). Organic matter (OM)-rich shales in the lacustrine Yanchang Formation are the major sources of oil in the Ordos Basin with proved reserves of about 30.75×10^8 t until 2012 (Yang et al., 2013), which is one of the most productive petroliferous basins in China. The Chang 7 Member of the Yanchang Formation (abbreviated to Chang 7 shale here) has recently been demonstrated as one of the most promising hybrid shale oil/shale gas systems in lacustrine strata in China (Loucks et al., 2017; Wang et al., 2014, 2016; Yang et al., 2013, 2016; Zhang et al., 2015a,b). The total porosity in this member has mainly been controlled by its clay mineral content (Fu et al., 2015; Jiang et al., 2016; Wang et al., 2015), which is consistent with the predominance of intraparticle pores in clay platelets and a relatively high clay mineral content (Loucks et al., 2017; Wang et al., 2016). The Chang 7 shale probably lacked early cementation during diagenesis, and thus the lithification was less developed, but the compaction effect was more extensive (Ko et al., 2017). In general, the average size of OM pores was found to be much smaller in the Chang 7 shale than in Eagle Ford marine shale (Ko et al., 2017); in addition, the sizes and types of interparticle pores show significant differences between the silty laminae and clayey laminae of the Chang 7 shale (Lei et al., 2015), which is related both to silt grain-size and sorting degree (Ko et al., 2017). Besides the Chang 7 Member of the Yanchang Formation, a few samples have also been investigated for the Chang 9 Member (Ko et al., 2017; Loucks et al., 2017), abbreviated to Chang 9 shale here, which is also rich in OM (Guo et al., 2014a; Zhang et al., 2007).

Shale within the oil window was affected by compaction, cementation and self-source oil infilling, which has greatly lowered the size and number of primary interparticle pores (Ko et al., 2016; Loucks and Reed, 2014; Löhr et al., 2015; Mastalerz et al., 2013; Pommer and Milliken, 2015). However, secondary pores within OM begin to develop during petroleum generation and subsequent expulsion as a combined result of hydrocarbon loss, volume change of residual organic solids, and exsolution of gases (Guo et al., 2017; Jarvie et al., 2007; Loucks et al., 2009, 2012; Löhr et al., 2015; Valenza et al., 2013). Most of the Chang 7 and Chang 9 shales from the southeastern Ordos Basin are in the oil window, as suggested by the range of vitrinite reflectance (VRo) values between 0.7% and 1.2% (Fu et al., 2015; Guo et al., 2014a; Jiang et al., 2016; Tang et al., 2014). Pores in the OM in Chang 7 shale have been commonly observed to be less developed than the intraparticle pores within clay and mica aggregates (Loucks et al., 2017; Wang et al., 2016); however, OM pores dominated the pore systems of many of the samples investigated (Ko et al., 2017). The major factors influencing the development of OM pores in the Chang 7 shale have not so far been elucidated in detail. Residual OM in the Chang 7 shale from the southeastern Ordos Basin is mainly solid bitumen (about 95% by volume of the total OM) and minor vitrinite, inertinite, alginite and waxy terrestrial liptinite (Hackley et al., 2017). Palynofacies analysis of the Chang 7 and Chang 9 shales from the central, southern and southeastern parts of the Ordos Basin has provided evidence that the shales are rich in *Botryococcus* algae, acritarchs and amorphous organic matter (AOM), with minor amounts of vitrinite and inertinite also present (Ji et al., 2006, 2009, Ji and Xu, 2007; Zhang et al., 2015a). The relationship between OM maceral type and OM porosity is not clear. Scanning electron microscopy (SEM) observations have been combined with low-pressure gas adsorption measurements in recent studies to gain an insight into the pore characteristics of the Chang 7 shale (Ko et al., 2017; Loucks et al., 2017; Wang et al., 2015). Nonetheless, possible linkages are yet to be established between the results of FE-SEM observation and those of low pressure gas adsorption for the OM pores in the shale.

In this study, the characteristics of pores, especially those in OM, were mainly described using SEM images of ion-milled surfaces of shale samples from both the Chang 7 and Chang 9 members. To gain an insight into the distributions of pores smaller than the SEM detection limits, and to quantitatively evaluate their characteristics, low-pressure

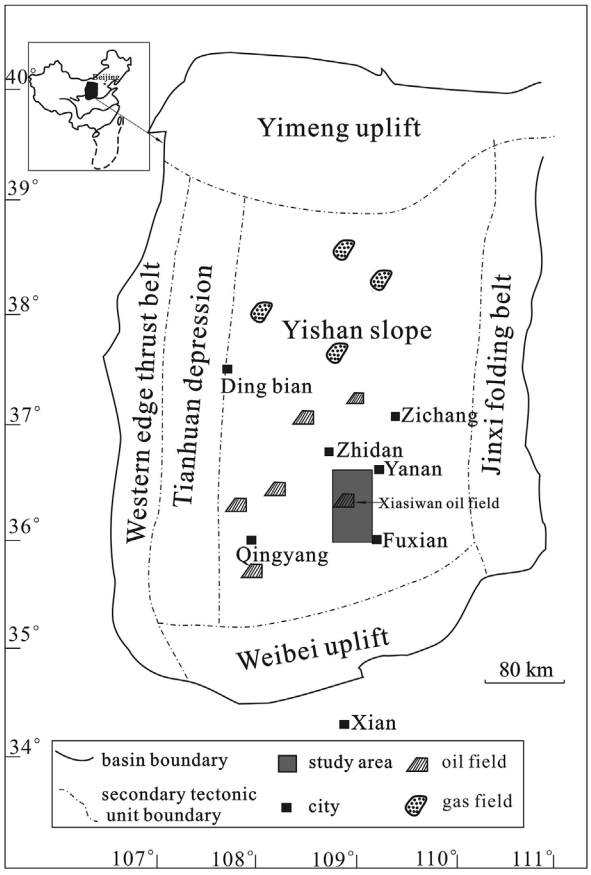

Fig. 1. Simplified map of the Ordos Basin showing major structural units and the distribution of oil and gas fields (modified after Guo et al., 2014a).

CO_2 and N_2 adsorption methods were used in pore-distribution analysis, along with mercury intrusion and helium pycnometry. Through the combined investigations, this study has tried to elucidate the relationships between OM maceral type and OM porosity and between FE-SEM observed pore characteristics and measured pore distributions by low-pressure gas adsorption, and finally to determine the main factors controlling OM pore development in the studied sample set.

2. Samples and experimental analysis

2.1. Geological backgrounds and samples

The geological backgrounds of a relatively large sample set from which the samples were selected in this study were introduced in Guo et al. (2014a). Briefly, the Ordos Basin is located in the western part of the North China Craton. The Ordos Basin is subdivided into six structural units: the Tianhuan Depression and Western Edge Thrust Belt in the west, the Jinxi Fold Belt in the east, the Yimeng Uplift in the north, the Weibei Uplift in the south and the Yishan Slope in the middle (Fig. 1). Continental deposition was initiated as a result of the Indosinian movement in the Late Triassic. The Yanchang Formation represents the whole lacustrine basin evolution and is separated into 10 members (Chang 10 to Chang 1 in ascending order, Fig. 2). The Chang 10 Member was developed early in lake formation, and is mainly composed of sandstone and sandy mudstone which were deposited in a fluvial environment. With continuous subsidence, the lake area became larger, and mudstones are present in the Chang 9 Member in the deep lake facies. The Chang 8 Member was also deposited during an expansion of the lacustrine basin. The Chang 7 Member was deposited during the peak stage of basin development when the water was deepest and the lake area was the largest. Thick black shales/mudstones

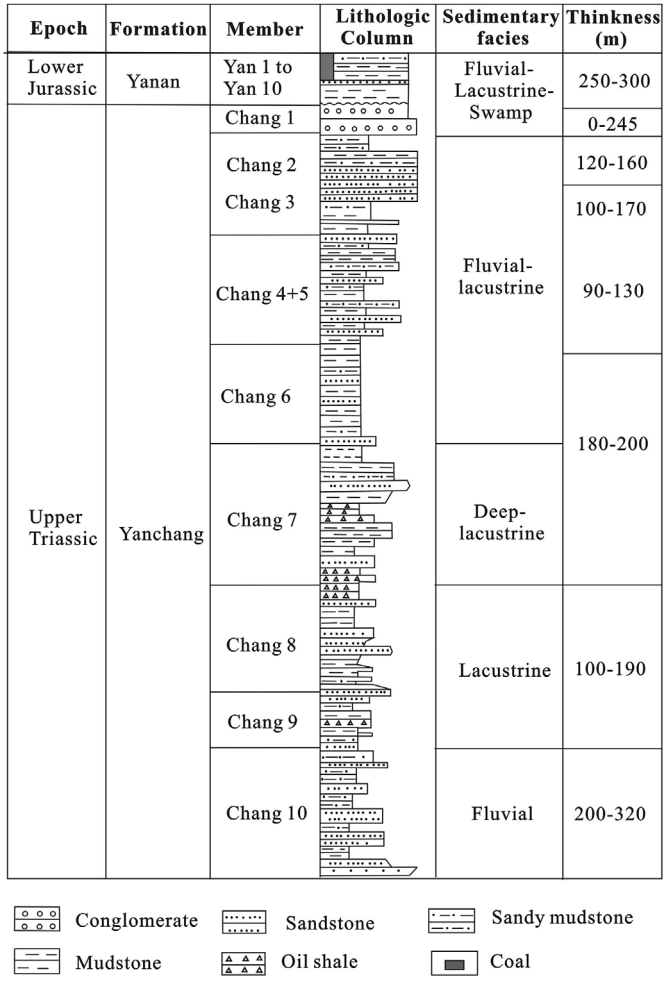

Fig. 2. Stratigraphic column in the study area. This Figure was modified after Guo et al. (2014a).

were widely developed in the deep lacustrine facies. During the deposition of the Chang 6 Member, the basin began to contract as sedimentation rate exceeded the subsidence rate. After that, the lake basin continued to grow smaller during the depositional stages of the Chang 5, 4 and 3 members. Tectonic uplift of the basin then caused the lacustrine area to contract significantly during the deposition of the Chang 2 Member. The Chang 2 and Chang 1 members were mainly deposited in a deltaic environment. Therefore, shales/mudstones are widely distributed in the semi-deep to deep lacustrine facies of the Chang 7 and Chang 9 members.

The study area was located in the southeastern Yishan slope, where the Chang 7 Member is about 50–110 m thick and the Chang 9 Member is 6–30 m thick (Wang et al., 2014). Samples from seven core wells used in the present study were selected from a relatively large sample set in this area (Guo et al., 2014a). Based on the mineral composition and organic geochemistry data of the large sample set reported in previous work, five samples were selected from each of the two members to investigate their pore characteristics (Table 1). The selected samples covered a total organic carbon (TOC) range of 2–10 wt%. Major minerals in the samples included quartz (26–44%), feldspars (8–29%) and clay minerals (27–52%), which were made up of illite/smectite mixed layers, illite, kaolinite, and chlorite, with illite/smectite being the major component (Guo et al., 2014a). The ten samples were organic-rich argillaceous mudstones, based on lithology classification schemes suggested by Ruppel et al. (2017) and Loucks et al. (2017) for the Yanchang shale. The OM in these samples was mainly type II (Fig. 3a). The Tmax value of selected samples varied from 429 °C to 465 °C. The amount of free hydrocarbons normalized to TOC content (the S1/TOC ratio, calculated based on Rock-Eval analysis) in the large sample set of Guo et al. (2014a) roughly showed a maximum value at the Tmax of 440 °C (Fig. 3b), which may indicate the peak of the oil window. Therefore, selected samples in this study varied in maturity from the early stage of the oil window, through the peak and late stage of the oil window, to the early wet gas stage.

2.2. Organic petrology

Maceral identification was performed on thin sections using a Leica MPV microscope in reflected and transmitted white light and fluorescent blue light. Some of the ion-milled areas in sample slabs were also observed in reflected white light and fluorescent blue light using a Leica MPV microscope.

2.3. Field emission-scanning electron microscopy (FE-SEM)

All the samples were investigated using a Hitachi S8010 SEM system equipped with secondary electron (SE) and backscattered electron (BSE) detectors. The areas of interest in each sample slab were sectioned and polished in a direction normal to the bedding by an Ar-ion milling instrument (Hitachi IM4000) to produce flat surfaces with minor topographical variation. Milling was conducted at accelerating voltages of 6 kV for 1.5 h and 4 kV for 0.5 h. Working distances during the FE-SEM observation ranged between 2.5 mm and 8 mm at a voltage of 1.5 kV. The detection limit was 5 nm. The size of pores and OM was measured using JMicroVision software. In most cases, the pore shape was irregular. The pore diameter was the equivalent circular diameter.

2.4. Low-pressure CO_2 and N_2 gas adsorption

Core samples were crushed to pass an 80-mesh sieve and dried in a vacuum oven at 110 °C for 24 h. The adsorption measurement was preceded by de-gassing the sample powder for 12–24 h to remove gases and moisture. CO_2 adsorption was performed on a Quantachrome NOVA 4200e analyzer at 0 °C and relative pressures (P/P_0) from 0.0005 to 0.03 to measure the micropore volume. Micropore volume (< 2 nm) and pore volume distribution with respect to pore diameter were determined using the density functional theory (DFT) model included in the software of the instrument. N_2 adsorption was carried out using a Micromeritics ASAP 2020 instrument at −196 °C for P/P_0 = 0.005 to 0.995 to measure the mesopores (2–50 nm) and some of the macropores (50–300 nm). Pore volume and distribution for pore diameters from 1.7 to 300 nm were derived using the Barrett-Joyner-Halenda (BJH) model (Barret et al., 1951).

2.5. Mercury intrusion analysis and bulk porosity determination

Sample cylinders ranging in diameter from 1 to 2 cm was used for the mercury intrusion analysis. Before the analysis, the samples were de-gassed and de-watered in a vacuum oven at 110 °C for 24 h. The mercury intrusion was conducted on a Micromeritics AutoPore 9510 mercury porosimeter. A contact angle of 130° (Gan et al., 1972) and a surface tension of 485 mN/m (Gregg and Sing, 1982) were adopted for the measurements. Applied pressures varied from 0.01 to 413 MPa, covering a pore-throat size range of 3 nm–120 μm. The pore-volume distribution with respect to the throat sizes was determined using the Washburn equation (Washburn, 1921). The bulk porosity of the shale was calculated from the difference between the bulk density (ρ_{bulk}) and the skeletal density ($\rho_{skeletal}$, the density of a solid material calculated by excluding the pore and void volume) using the formula [porosity = $(1-\rho_{bulk}/\rho_{skeletal}) \times 100$] (Tian et al., 2013). Mercury immersion measurement allows both the bulk density and skeletal density to be determined. The skeletal density was also determined by helium pycnometry at pressures less than 1.4 MPa on a Temco UltraPore-300

Table 1
Geochemical parameters, pore volume, density and porosity of selected Chang 7 and Chang 9 Member samples.

Sample [a]	Well	Depth	TOC	S1	S2	Tmax	Pore volume (cm^3/100 g)			Bulk density	Hg-skeletal density	He-skeletal density	He-Hg porosity	Hg-porosity
		(m)	(%)	(mg/g)	(mg/g)	(°C)	< 2 nm	2-50 nm	50-300 nm	(g/cm^3)	(g/cm^3)	(g/cm^3)	(%)	(%)
C7-6	X-6	1736.36	7.2	9.62	23.44	441	0.02	1.38	0.97	2.341	2.409	2.461	4.88	2.82
C7-11	X-11	1315.1	5.74	4.56	14.71	442	0.12	0.98	0.97	2.393	2.43	2.458	2.65	1.53
C7-12	X-12	1140.03	3.7	3.55	8.02	436	0.11	1.06	0.82	2.652	2.656	2.671	0.72	0.14
C7-13	X-12	1149.74	4.25	4.77	11.63	434	0.11	0.89	0.89	2.422	2.486	2.512	3.57	2.55
C7-25	X-15	1846.62	7.68	3.88	15.16	448	0.22	1.08	0.78	2.361	2.432	2.445	3.42	2.9
C9-27	X-2	1124.28	2.02	0.42	1.92	465	0.21	1.39	1.1	2.541	2.624	2.675	5.01	3.18
C9-30	X-19	1179.89	2.06	1.78	4.68	429	0.01	0.96	1.27	2.511	2.531	2.538	1.08	0.79
C9-32	X-18	1402.33	9.74	1.96	15.35	458	0.7 [b]	0.25	0.44	2.335	2.396	2.435	4.11	2.56
C9-35	X-12	1306.34	8.39	3.71	13.26	456	0.22	0.75	0.65	2.39	2.444	2.438	1.99	2.22
C9-37	X-12	1308.11	4.65	3.12	8.19	449	0.02	1.49	1.18	2.401	2.481	2.572	6.67	3.26

[a] C7, C9 abbr. Chang 7 and Chang 9. Geochemical parameters, i.e. TOC, S1, S2 and Tmax, have been reported by Guo et al. (2014a).
[b] Micropore volume of sample C9-32 after Guo et al. (2014b).

instrument (Core Lab, USA).

3. Results

3.1. Organic petrology

Solid bitumen was the most common OM type in the selected samples, over a large range of both TOC content and maturity (Fig. 4). Type III kerogen, vitrinite, was a minor OM component in the studied samples. Inertinites were also observed. Fluorescent liptinite, such as alginite, were generally observed in most of the high-TOC samples. Recent studies of the organic petrology of North American marine shales and the Yanchang lacustrine shale have shown that solid bitumen dominated the OM of shales in the oil window (Hackley and Cardott, 2016; Hackley et al., 2017). Maceral observations performed in the present study are consistent with their conclusion. Moreover, the distribution of liptinites in any given shale sample was very heterogeneous.

Solid bitumen in relatively low-TOC samples generally appeared to have a string-like shape, or to a lesser extent an irregular shape (6–40 μm in size, Fig. 4a and b). In samples with relatively high TOC content, solid bitumen was larger (up to 500 μm in length) and more abundant (Fig. 4c, d, g–i), and has string, stripe or band-like and irregular shapes (Fig. 4c, d, h, i). These may suggest that they were generated and migrated out of kerogen, and infilled the pores or cracks between minerals. Sample C9-32 is characterized by very abundant solid bitumen laminae which are mostly interconnected. This was most evident in fluorescent light (Fig. 4j).

Elliptical or granular alginite, although rarely observed, show yellow or orange colors in fluorescent blue light (Fig. 4b, j), with a diameter of 15–70 μm. They could not be differentiated from the mineral matrix under reflected light but were evident in fluorescent blue light (Fig. 4c, d, i, j). Relatively small yellow liptinite particles (2–15 μm), normally having irregular shapes, were tentatively thought to be alginite fragments (Fig. 4d, f, j). In addition, some greenish-yellow liptinites of undetermined type and dark brown mineral bituminous groundmass can also be observed. Sample C9-37 is notable for relatively wide but heterogeneous distributions of liptinite (mostly yellow alginite, Fig. 4e and f). A large amount of macro-algae lamina remnants more than 600 μm long and 10–100 μm wide were present (Fig. 4e), along with isolated, irregularly shaped alginites (30–80 μm long, Fig. 4f) and very small alginite fragments.

Vitrinite and inertinite mostly have straight edges (Fig. 4a, g, i): vitrinite commonly had irregular shapes; in contrast, inertinite with bogen structure (arc-shaped fragments of preserved cell walls) were usually observed (Fig. 4a). However, inertinite with cell lumens was not found in this work. Vitrinite ranged from 10 μm to 35 μm in length and from 4 μm to 10 μm in width; inertinite particles were slightly smaller.

3.2. Pores developed within OM

Pores within OM are subdivided into four subtypes, depending on the degree of pore development. They are non-developed, poorly developed, well developed, and excellently developed respectively. An

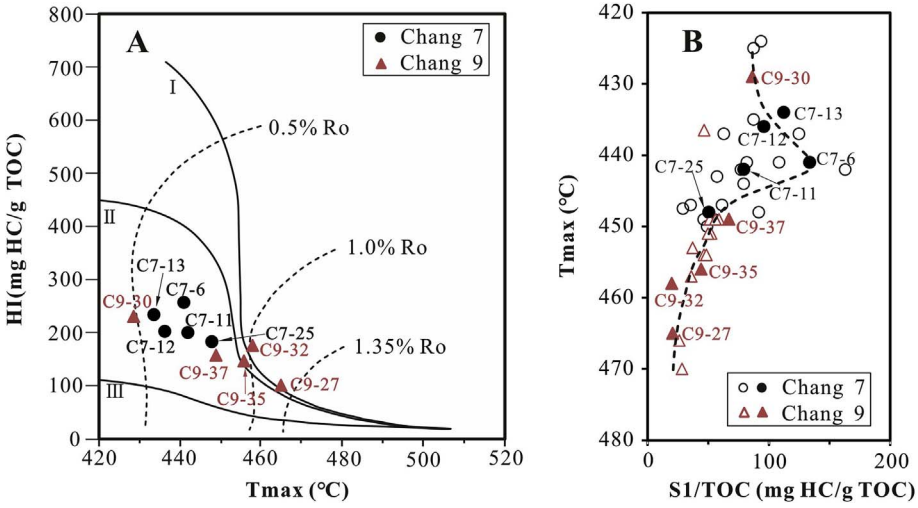

Fig. 3. (a) Tmax vs. HI showing the OM type and thermal maturity levels of selected samples. (b) S1/TOC vs. Tmax (filled circles and triangles stand for samples chosen in this paper). Data plotted in this Figure from Guo et al. (2014a).

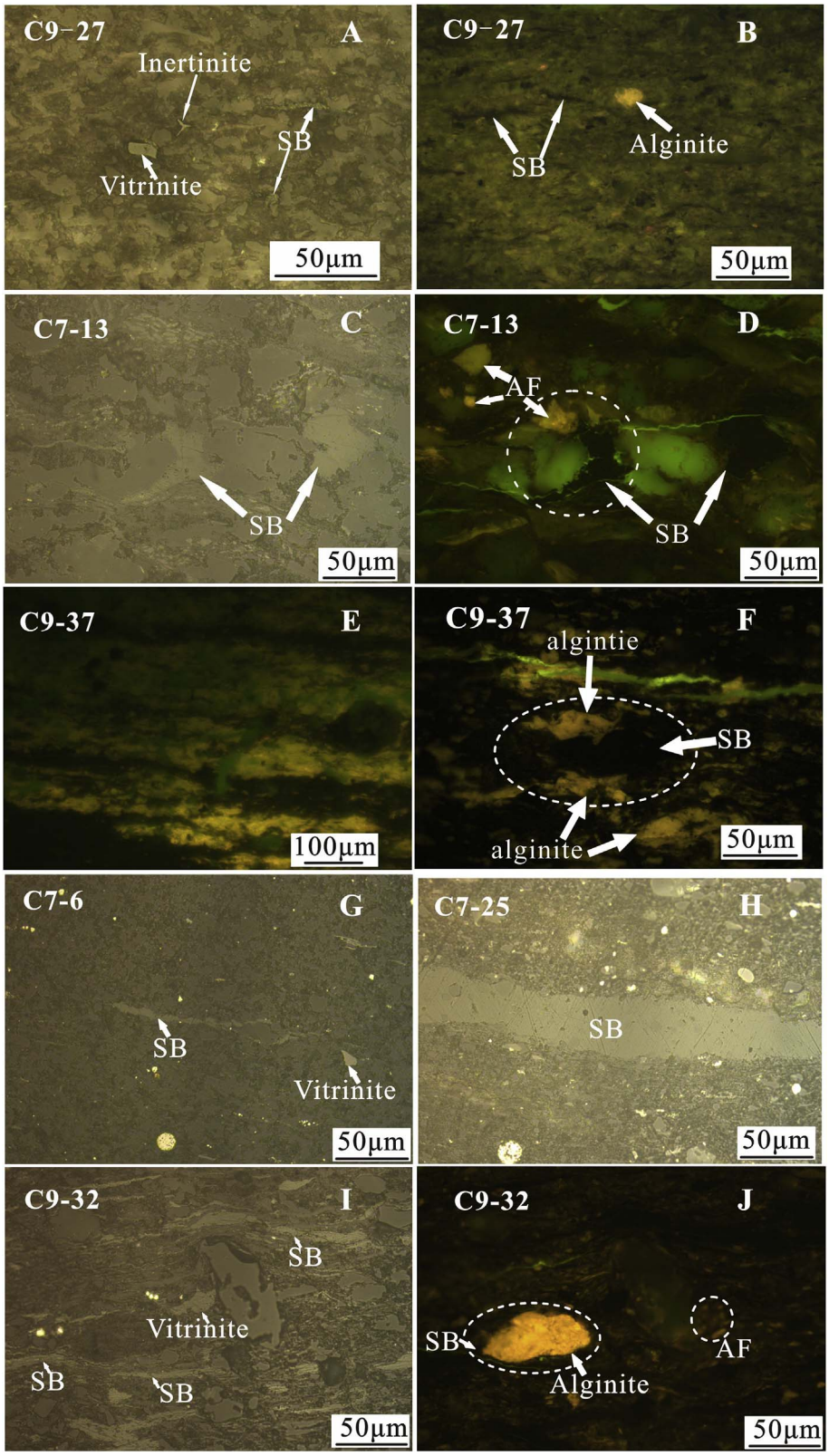

Fig. 4. Thin-section photomicrographs in reflected light (a, c, g–i) and fluorescent light (b, d, e, f, j). Panels (d) and (j) are areas (c) and (i), respectively, also photographed in fluorescent light. AF = alginite fragments; SB = Solid bitumen.

attempt was made to study the pore development in specific OM macerals. This is a very difficult task because SEM images of ion-milled surfaces reliably distinguish OM from minerals, but do not easily permit the characterization of the OM. Previous studies (Loucks and Reed, 2014; Loucks et al., 2012; Lu et al., 2015; Milliken et al., 2013) have suggested several criteria for recognizing woody material (deposited OM) and solid bitumen (migrated OM), mainly based on the relationship between OM and minerals and the shape and edge characteristics of OM in shale. However, maceral types such as liptinites, vitrinite and inertinite can only be recognized with low confidence. Although the characteristics of macerals introduced in section 3.1 can help in judging the maceral types in SEM images, many uncertainties still exist: for

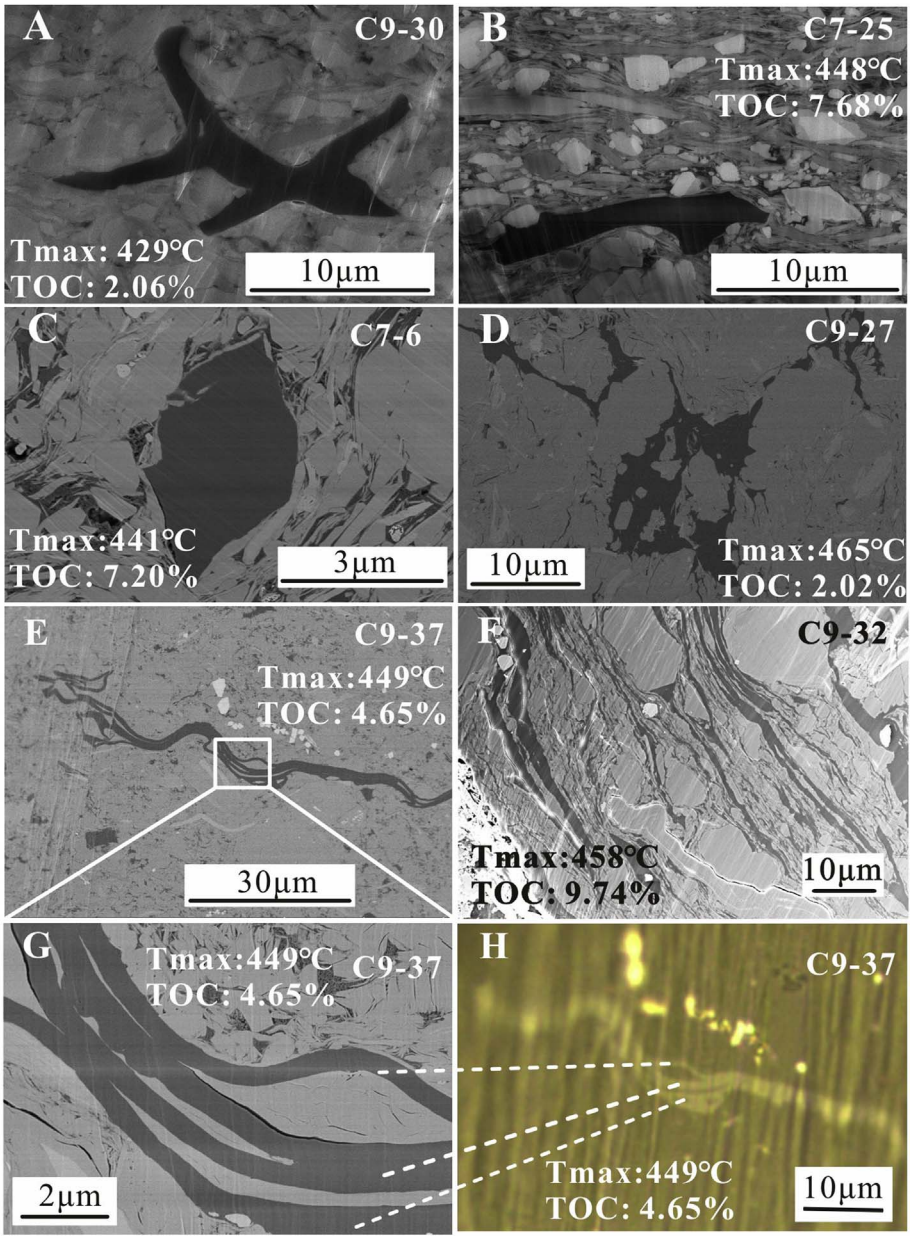

Fig. 5. OM without visible pores in the Chang 7 and Chang 9 shales. (For more information about samples, please refer to Table 1). Panel h was taken in reflectance white light using light microscopy.

example, liptinites and solid bitumen display relatively large variations in shape (stripe-like, irregular with sharp boundaries, etc.). In addition, the shapes of relatively small macerals (< 10 μm) are poorly defined in light microscopy, but they can be clearly seen in SEM images of ion-milled surfaces. More importantly, when different types of organic maceral cohere (e.g. the solid bitumen and alginite in Fig. 4d, f, j) they appear as a single, undifferentiated piece of OM in SEM images. This may be common in shales with medium to high TOC content.

3.2.1. No visible pores within OM from various sources

Woody OM derived from higher plants was tentatively identified in the studied samples (Fig. 5a–c), mainly on the basis of particle shape (e.g., arcuate), sharp boundaries and subtle curvature along their edges (Loucks and Reed, 2014; Loucks et al., 2012; Lu et al., 2015; Milliken et al., 2013); Fig. 5a shows one typical example that is probably inertinite, based on light microscopic observation. These particles vary greatly in both size and shape. Some are irregular polygons measuring ~3 μm (Fig. 5c), while others are seen as irregular band- or belt-like shapes 10–20 μm long and 3–5 μm wide (Fig. 5a and b).

Some OM that has infilled pre-existing interparticle pores or microfractures was found to be non-porous (Fig. 5d–g). Most occurred in elongated or irregular polygon-like shapes, depending on the boundaries of the surrounding minerals (Fig. 5d). The OM varied greatly in size ranging from tens of nanometers to about 100 μm with most of them in tens of micrometer scale. Their shape and relationship with minerals suggest that this OM was solid bitumen that had migrated into interparticle pores or microfractures (Fig. 5d and e), adopting the criteria suggested by Loucks and Reed (2014). The relatively long solid bitumen in sample C9-37 (Fig. 5e) is notable for the shape of the left-hand end and the middle part. The shape of this OM suggests that it may be a liptinite, such as an algal spore (Milliken et al., 2017). However, the multiple-laminate structure in the middle part was grey in reflected light (Fig. 5h), which supports its classification as solid bitumen.

Well-developed OM laminae were observed in the highest-TOC sample (C9-32, Fig. 5f), consistent with abundant solid bitumen imaged using light microscopy (Fig. 4i and j). The OM laminae were interlayered, mostly with clay minerals and less frequently with rigid

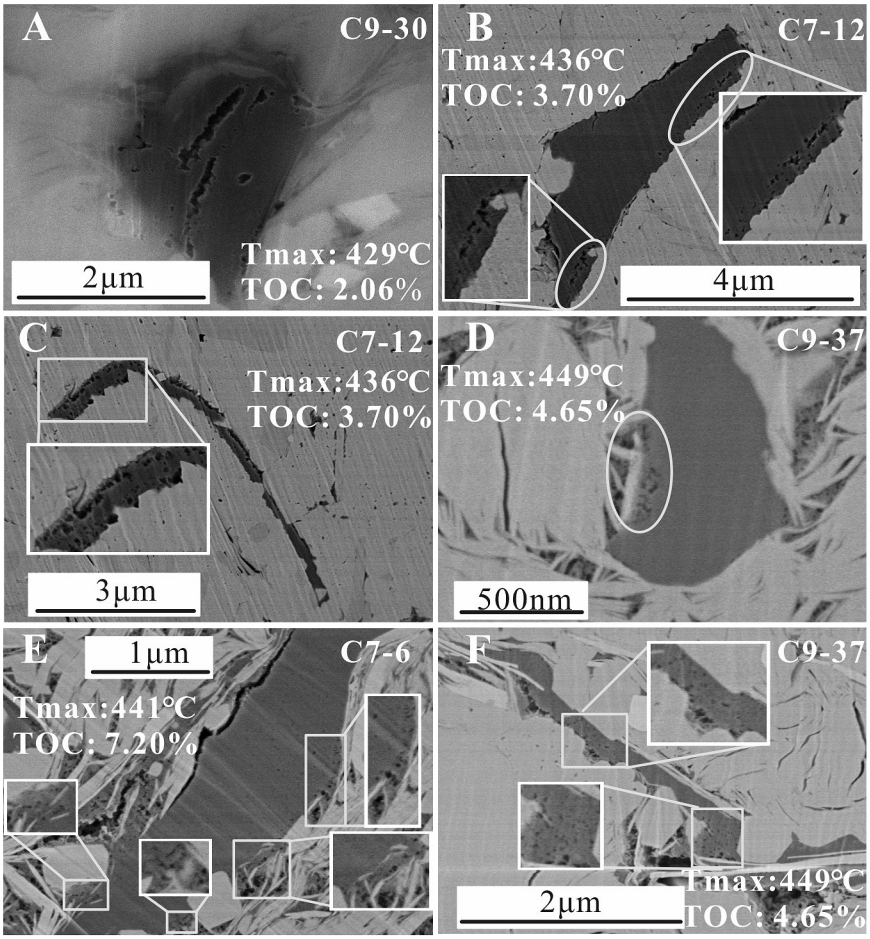

Fig. 6. Poor development of pores within OM.

minerals such as euhedral quartz or pyrite crystals; these appeared throughout the ion-milled region (> 100 μm). Close contact between solid bitumen and fluorescent liptinite was normal in this sample (Fig. 4i and j), which suggests that these liptinites were also non-porous.

3.2.2. Poor development of pores within OM

The surface porosity, defined as the ratio of pore area to OM area, was measured using JMicroVision software. The values ranged between 0.9% and 10.5% (Fig. 6). Pores with sizes of 10–100 nm were roughly round or elliptical in shape. Most of the pores were aligned along the OM rim or parallel to the rim (Fig. 6a–c), while others were randomly clustered within small zones close to the rim (Fig. 6 d–f). These pores were sometimes linked, especially the former, forming a microfracture similar to that in Fig. 6a, and usually less than 0.5 μm long. Fig. 6a shows a very small, quasi-polygonal OM with slit-shaped, rough-edged pores about 1 μm long. Similar pores were reported in a sample of solid bitumen in a Cretaceous shale (VRo = 0.78%), and explained as devolatilization cracks, which might not exist in situ (Loucks and Reed, 2014). This type of OM was generally small in size with most of them less than 5 μm. Most of this type of OM was recognized as solid bitumen filling interparticle pores between minerals (Fig. 6b–c, e); others with sharp boundaries may be remnants of woody OM and thus deposition-related, as discussed above (Fig. 6a, d).

3.2.3. Good-to-excellent development of pores within OM

The surface porosity for the OM with good pore development was between 9.5% and 36.9% (Fig. 7). Well-developed pores within OM are described by the pore classifications suggested by Milliken et al. (2013): isolated and discrete, sponge-like and complex pores. Most isolated sponge-like pores (Fig. 7a–g) were roughly round, elliptical or elongated, varying in size around a few tens of nanometers (mostly smaller than 50 nm). Discrete sponge-like pores (Fig. 7a–e) were generally irregular or elongated in shape, and usually between 30 and 80 nm in size, but exceeding 100 nm in some cases. Some discrete pores may have formed when isolated pores have combined. Relatively large complex pores were also identified in OM macerals in which sponge-like pores were also evident (Fig. 7e–h). These pores were either connected or isolated, and were roughly round, elliptical (Fig. 7e, h) or irregular (Fig. 7g). The pores lay mainly within the size range of 400 nm, but were as large as ~700 nm. Small pores have previously been reported within pores larger than 200 nm (Milliken et al., 2013), and were clearly seen in the present study (Fig. 7g and h). Complex pores were common in two medium-TOC samples (C7-6 and C9-37) but were only occasionally seen in other samples.

Significant OM pore development was observed in sample C9-37 (Fig. 8). The clearly visible sponge-like structure (Fig. 8b) indicates intense pore development. Overall, this type of OM was characterized by cross-linked network of organic fibers or bridges. This type of OM was smaller than 10 μm, with pores varying greatly in size, mostly between 10 and 120 nm, and occasionally up to 250 nm. Relatively small pores with diameters of 20–50 nm were generally elliptical or irregular in shape; medium-sized pores (50–120 nm, commonly observed in the sample) were mostly elliptical. The irregular shape of pores larger than 120 nm might have resulted from the breakage of nanofibers separating smaller pores. The nanofibers separating pores varied from 7 to 34 nm in width, with a main width range of 10–20 nm. The surface porosity of sponge-like OM was calculated to be as high as 40% (Fig. 8a) based on pore identification and statistical data.

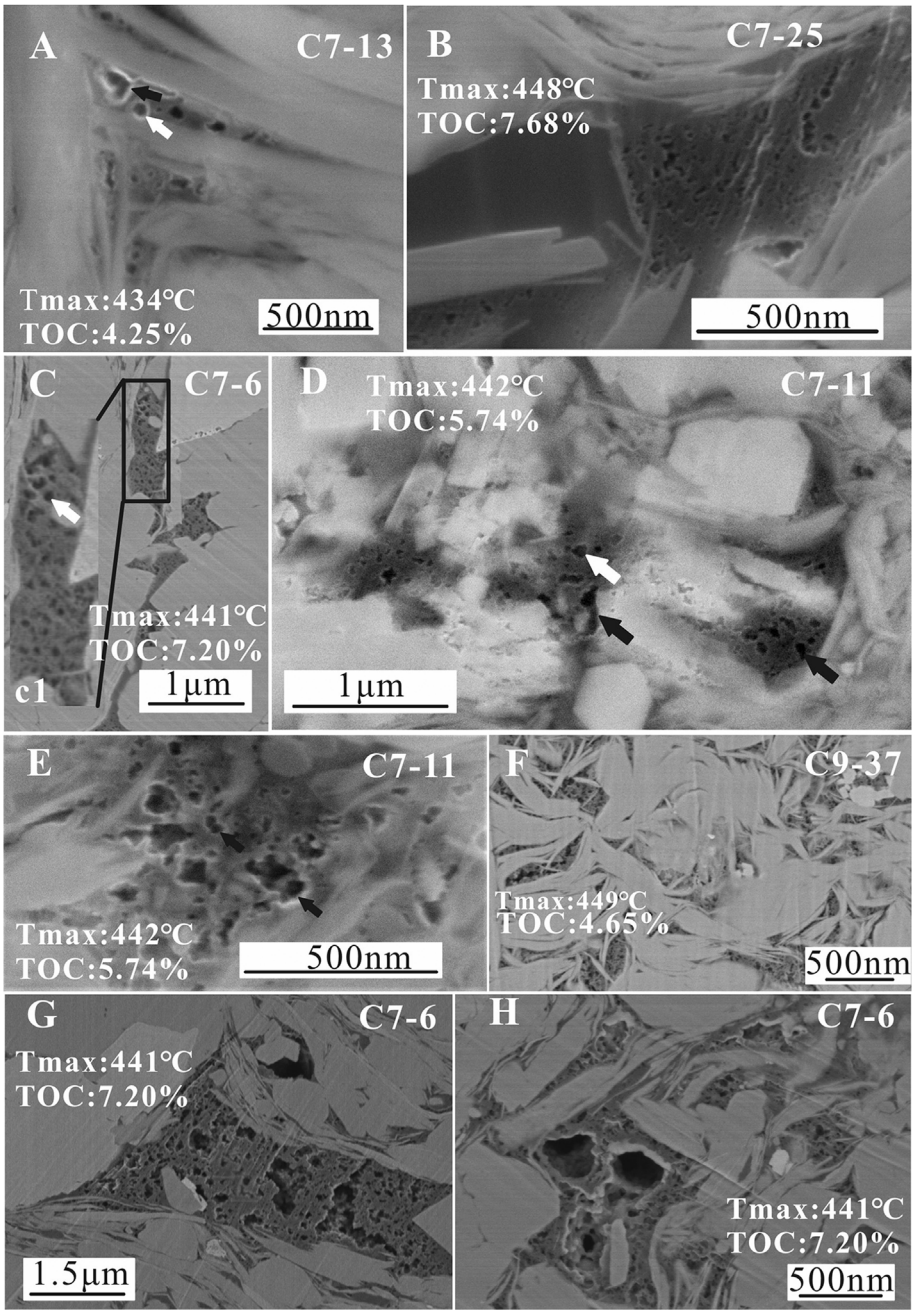

Fig. 7. Well-developed pores within OM. White arrows indicate isolated spongy pores; black arrows indicate discrete spongy pores.

3.2.4. Microfractures associated with OM

Different types of microfractures were identified within the OM (Fig. 9), some of which also appear above in Fig. 6a. Microfractures in OM without visible pores usually had smooth walls, either straight or curved, and from one to a few micrometers long (Fig. 9c and d). The OM was solid bitumen infill between minerals (Fig. 9c and d) and appeared as irregular strips. The microfractures generally cut across the OM and have developed either along the OM-mineral boundary or perpendicular to it (Fig. 9c and d).

Microfractures were also observed in OM with significant development of spongy and complex pores (Fig. 9a and b), some with rough rims within the OM (Figs. 6a and 9a–b). Most of these fractures were less than 2 μm long, and seem to have formed by the coalescing of small, isolated pores.

A third type of microfracture in the Yanchang shale was typically parallel or sub-parallel to the bedding (Fig. 9e and f), some with migrated bitumen infill (Fig. 9e). Such fractures were typically more than tens of micrometers long. In sample C9-32, with virtually no visible OM pores, fractures from 4 μm to 80 μm long were seen (Fig. 9f).

Microfractures in shale may be generated by various processes, possibly due to the drying of clay minerals and consequent shrinkage, either during the lifting of cores or in sample preparation (Loucks and Reed, 2016, Fig. 9d–f). Microfractures in the OM might result from the devolatilization of solid bitumen and pyrobitumen, the rims of which may be either smooth or rough (Fig. 9c and d; Ko et al., 2017; Loucks and Reed, 2014, 2016; Loucks et al., 2017). Such microfractures might not exist in situ, however, as they are generated by devolatilization which occurs when the sample is released from the high subsurface pressure and temperature. High pressures could be created by the generation of oil and gas in shale. This occurs because the volume of the hydrocarbons exceeds that of the kerogen, generating elevated pressure during the maturation process. Sufficiently high pressure causes the shale to fracture, facilitating the flow of bitumen. This may explain the observation that some fractures are filled with solid bitumen parallel to

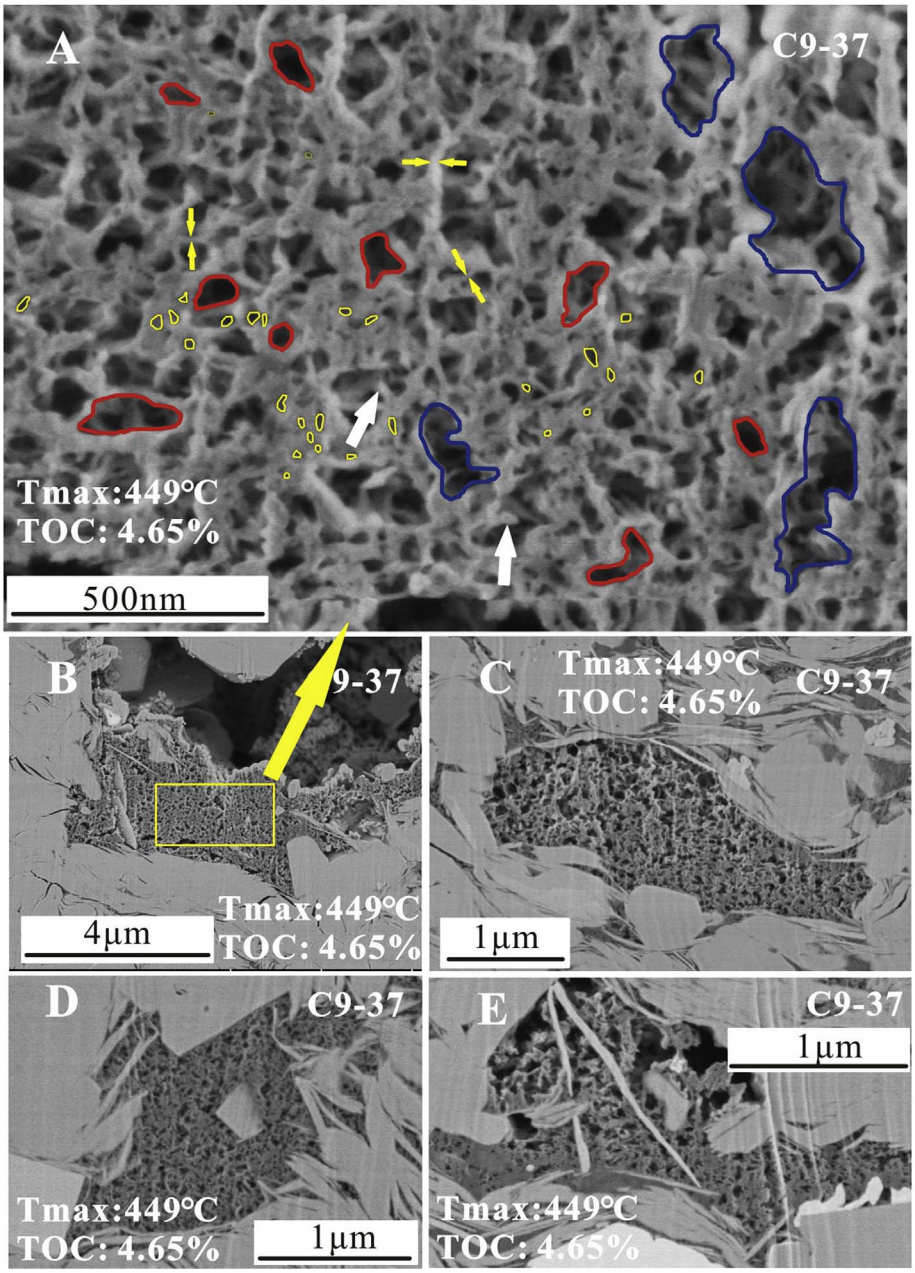

Fig. 8. Dense development of pores in OM showing a nanofiber structure in sample C9-37 (TOC content 4.65 wt%). The yellow, red and blue outlines show pores 10–50 nm, 50–120 nm and 120–250 nm long, respectively. White arrows indicate broken nanofibers or bridges separating pores. Small yellow arrows indicate nanofibers separating pores. (For interpretation of the references to color in this figure legend, the reader is referred to the Web version of this article.)

the bedding planes (Fig. 9e). Other factors (e.g., tectonic stress) could also lead to fracturing in the shale.

3.2.5. Pores in residual bitumen in shale

Pores with round, elliptical and irregular shapes in the residual bitumen were formed by oil evaporation/expulsion or modified mineral pores (Fig. 10). Most of the round and elliptical pores were a few hundreds of nanometers across (Fig. 10); irregularly shaped pores varied in size from one to a few micrometers. Macropores in the residual bitumen all had smooth rims that readily distinguished them from other types of OM pores. Moreover, the minerals submerged under the bitumen were clearly coated by an oil film. Similar pores in solid bitumen measuring a few hundreds of nanometers have been reported in mature shale (VRo = 0.78%, Loucks and Reed, 2014), which they interpreted as being associated with two-phase fluid inclusions — the two phases possibly being heavy oil/light oil, or oil/water, or oil/gas.

3.3. Pores associated with minerals

Pores associated with minerals were classified into three sub-types in the present study: intraparticle pores associated with clay minerals; interparticle pores; and intraparticle pores related to the dissolution process. The clay mineral content is relatively high in the Chang 7 and Chang 9 shales (mostly between 30% and 50%: Guo et al., 2014a). Well-developed pores in the aggregated clay platelets generally appeared as elongated, slit-like shapes parallel to the clay sheet (Fig. 11a and b). Most of the pores measured from hundreds of nanometers to several micrometers long, and up to 200 nm wide. Oil infill in clay aggregates is common in shales with high hydrocarbon generation potential (Fig. 11b).

Interparticle pores (Fig. 11c and d) between ductile clay minerals and rigid minerals (quartz, feldspar) were common, and were mainly associated with the compaction-resistant effect of the rigid minerals. These pores appeared as regular polygons with straight rims, or irregular shapes with straight and/or arcuate edges, depending on the

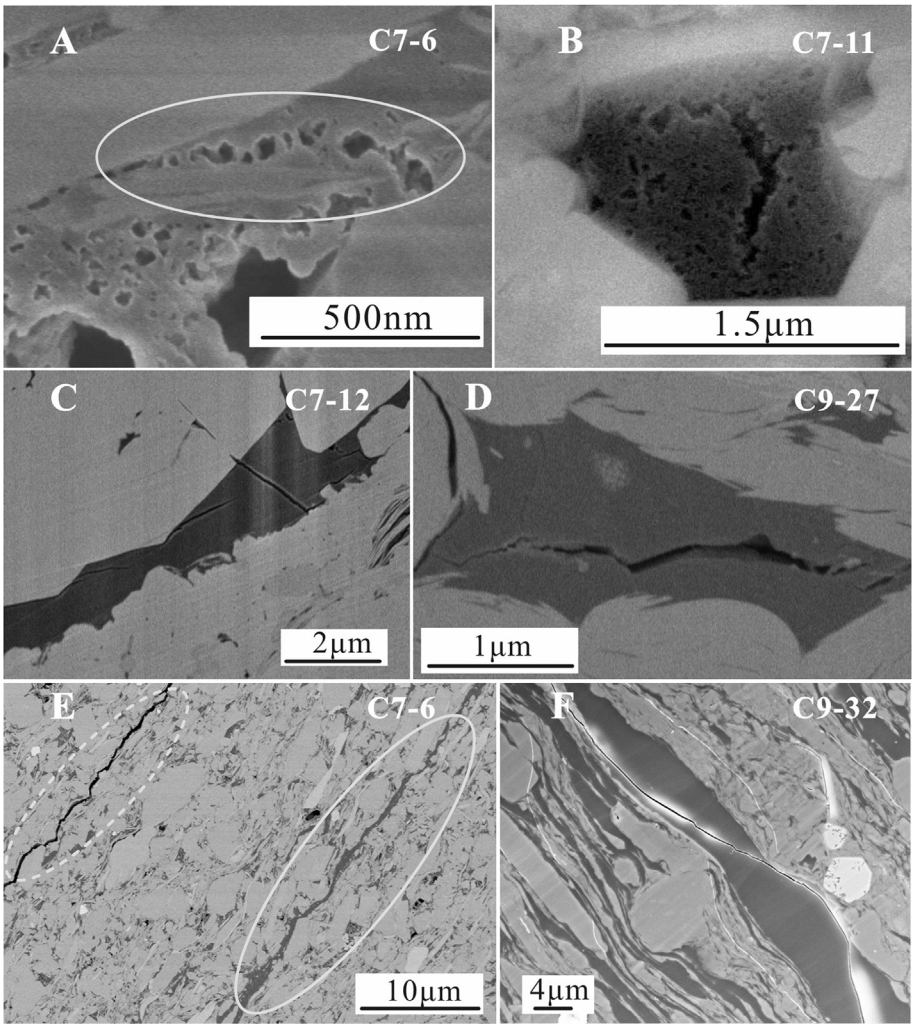

Fig. 9. Microfractures in OM. The fractures in panels e, f are some tens of micrometers long. Solid-line ellipses indicate fractures with bitumen infill; dotted-line ellipses indicate open fractures.

surrounding minerals. Such pores were relatively large — mainly between 100 nm and more than 1 μm.

Intraparticle pores are associated with dissolution; Fig. 11e shows a typical pore of this type, where the edges of the rectangular mineral particle (4 × 3 μm) have almost been dissolved, and the particle walls thus displayed saw-tooth rims. The particle in Fig. 11e was unconnected to OM. Significant dissolution had taken place at its corners, producing well-developed intraparticle pores. Dissolution also occurred when the mineral particle was surrounded by solid bitumen as shown in Fig. 11f, but in this case the pore development was limited to only a few parts of the mineral in contact with the bitumen. It is also notable that the solid bitumen was very porous. The size of the dissolution-related pores in the mineral particle ranged from 20 to 150 nm, although most were mesopores (Fig. 11f). It could also be observed that the K-feldspar has been partly displaced by albite (Fig. 11e and f). Dissolution is usually related to fluids resulting from the decarboxylation of kerogen, producing carboxylic and phenolic acid, which has taken place prior to oil generation (Schieber, 2010).

3.4. Pore characteristics revealed by low-pressure gas adsorption

3.4.1. CO_2 adsorption

The CO_2 adsorption isotherms for the shale samples of Chang 7 and Chang 9 members (Fig. 12) were type I, implying microporous solids with a relatively small external surface area (Sing, 1985). Most of the samples in this study had a relatively low CO_2 adsorption capacity (0.18–0.60 cm^3/g at relative pressure P/P_0 = 0.03); however, sample C9-32, with the highest TOC content (9.74 wt%), had a much greater

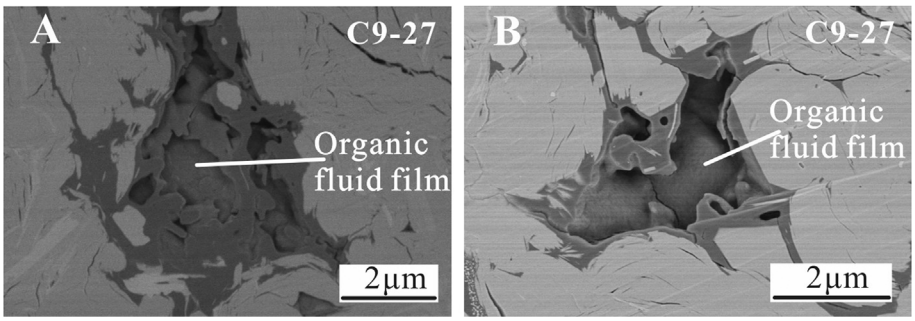

Fig. 10. Large pores within the residual bitumen filling interparticle spaces.

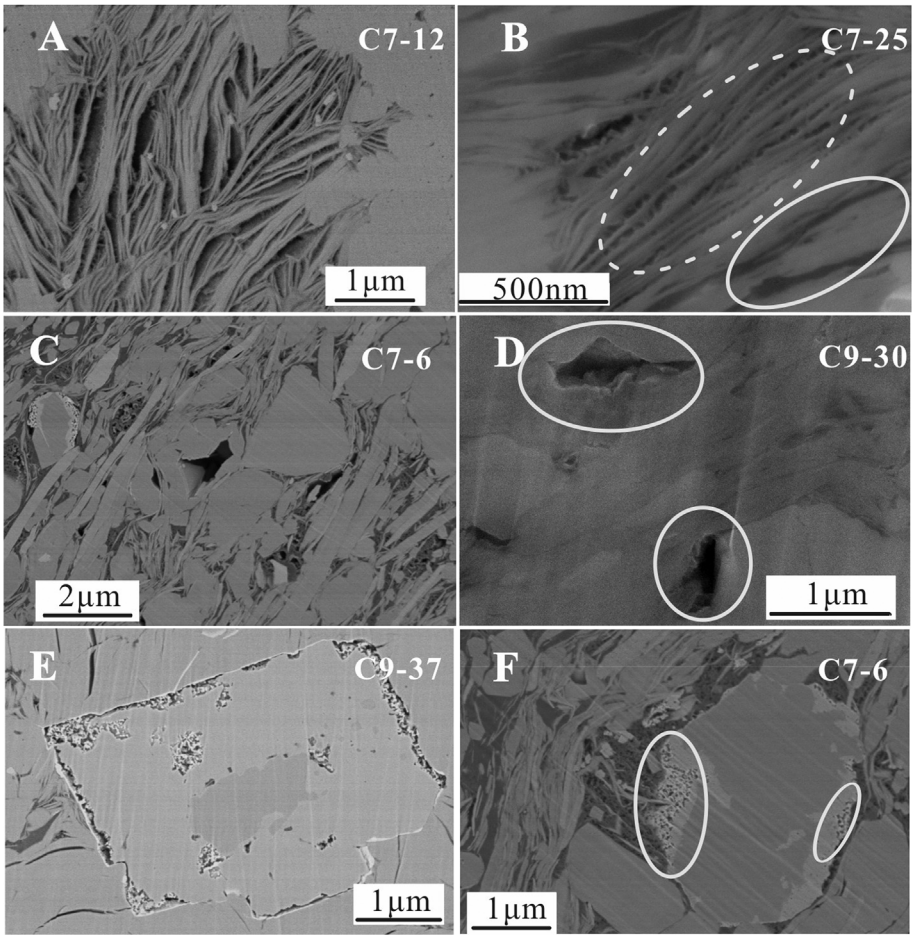

Fig. 11. Pores associated with minerals: (a, b) intraparticle pores associated with clay minerals or muscovite; (c, d) interparticle pores related to various minerals; (e, f) intraparticle dissolution pores in carbonate and feldspar. In panel b, the dashed outlines highlight unfilled pores between clay minerals, and the solid outlines are pores filled with OM.

adsorption capacity than the other samples (up to 2.0 cm^3/g, Fig. 12b). No clear correlation was found between CO_2 adsorption capacity and TOC content in the 10 samples investigated. In addition, samples C7-6 and C9-37 showed excellent growth of visible OM pores, but both had a very low CO_2 adsorption capacity (Fig. 7f–h, 12).

3.4.2. N_2 adsorption

The N_2 adsorption isotherms for all selected samples (Fig. 13) were type IV. Variation in adsorption capacity was much greater for the Chang 9 shale than for the Chang 7 shale. It is again notable that sample C9-32, with the largest TOC content and CO_2 adsorption capacity (Fig. 12b), had the lowest N_2 adsorption capacity (Fig. 13b), indicating limited development of pores in the 2–300 nm range; this is consistent with the fact that almost no pores were visible (Fig. 5f). Sample C9-35 (TOC = 8.39 wt%) had a higher N_2 adsorption capacity than sample C9-32, despite the fact that C9-35 was slightly less enriched in OM (Fig. 13b).

The pore-volume distribution of Chang 7 samples was unimodal within the diameter range of 1.7–300 nm, with a broad maxima between 10 and 100 nm. Pore volumes for different size ranges were generally similar for samples with distinctly different TOC contents (Fig. 14a; Table 1); however, sample C7-6, with the relatively higher

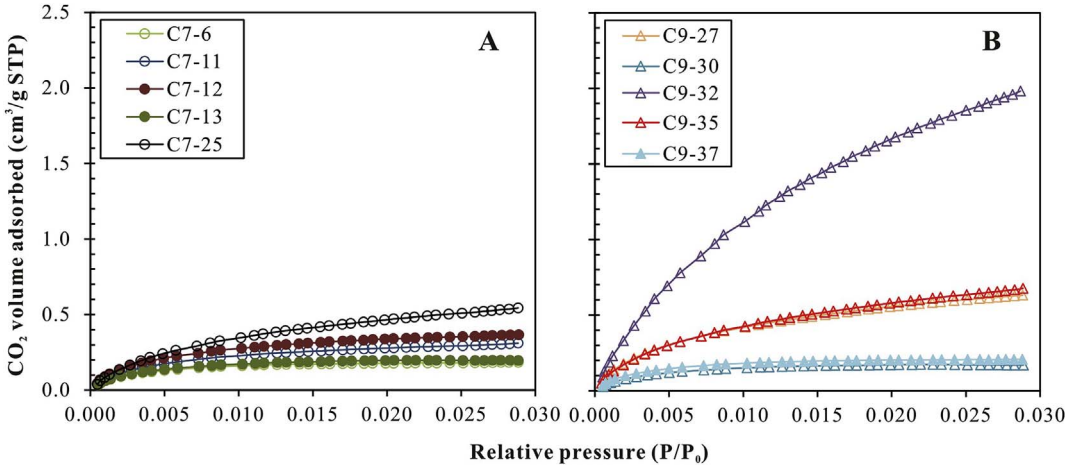

Fig. 12. CO_2 adsorption isotherms for (a) Chang 7 and (b) Chang 9 shales. (Isotherms for samples C7-13 and C9-32 after Guo et al., 2014a).

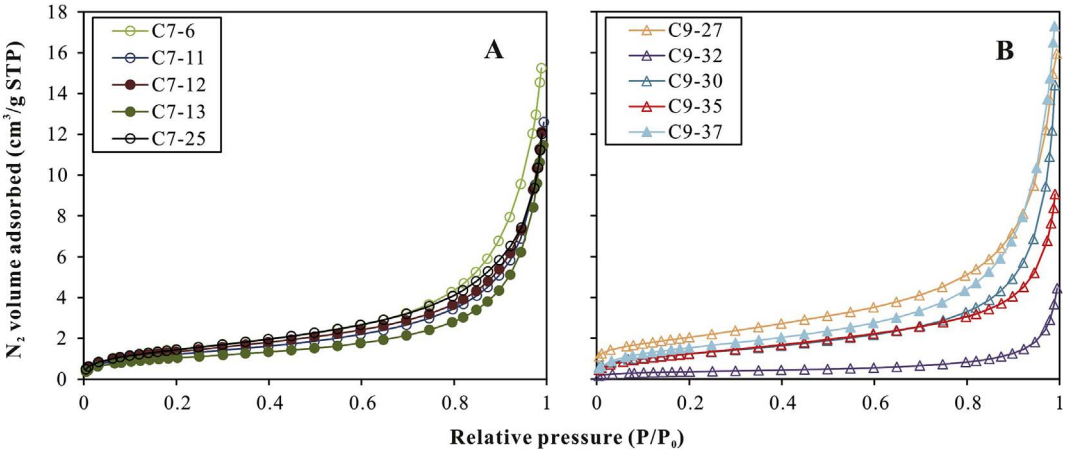

Fig. 13. N_2 adsorption isotherms for (a) Chang 7 and (b) Chang 9 shales. (Isotherms for sample C9-32 after Guo et al., 2014b).

TOC content of 7.2 wt%, showed a much greater pore volume than the other Chang 7 samples, between 10 and 60 nm, with a maxima at 30 nm. By contrast, all five Chang 9 samples showed considerable variation in their pore-volume profiles, although a broad maxima between 10 and 100 nm was also present (Fig. 14b). Samples C9-27 and C9-35 showed an additional peak maxima 3 nm, possibly related to the presence of clay minerals (Kuila and Prasad, 2013), and suggests that the mesopores between the clay aggregates were not fully filled by OM (Kuila et al., 2014). Three of the five Chang 9 samples with relatively lower TOC contents (C9-27, C9-30 and C9-37) had a much larger peak in the 10–100 nm range, implying greater volumes of both meso- and macropores than the other two high-TOC samples (C9-32 and C9-35; Table 1).

An interesting finding was that the pore volume in the 2–300 nm range displayed an approximately non-linear decreasing trend with increasing TOC content, with two exceptions (Fig. 14c). In detail, the two samples with TOC content of about 2 wt% had a pore volume of 2.23–2.49 cm^3/g in the 2–300 nm range. The pore volume was generally similar (1.78–1.95 cm^3/g) over the TOC range of 3.7–7.68 wt%, which is lower than that of the two lowest TOC samples. With increases in TOC content up to 9.74 wt%, the pore volume of samples C9-35 and C9-32 significantly decreased. The two exceptions were C9-37 and C7-6, which were observed to contain an abundance of relatively large OM pores (Fig. 7).

3.5. Pore-throat distribution and total porosity

The mercury intrusion technique measures the pore throat distribution of the samples. As Fig. 15 shows, the pore throats of both Chang 7 and Chang 9 samples were very small (most are smaller than 10 nm). The artificial intergranular porosity created during analysis preparation (e.g., shrinkage cracks in clay minerals or OM) may have contributed to the number of pores between 10 and 100 μm (e.g., the fractures in sample C9-32). The pore volume and pore size shown by SEM and N_2 adsorption are larger than those determined by mercury intrusion measurement, indicating that the connectivity of pores in the Yanchang shale, and therefore its permeability, is relatively poor. It has been noted previously that the Yanchang shale has an overall low permeability (Loucks et al., 2017).

The skeletal density was determined by both He pycnometry and mercury intrusion; the bulk density was determined by mercury intrusion. These produced two kinds of total porosity. The skeletal density and bulk density in Fig. 16a and b are similar, both decreasing as TOC increased. Fig. 16c and Table 1 show that the He-Hg porosity was apparently greater than Hg porosity, for the reason that helium molecules enter pore throats as small as 0.26 nm, whereas the smallest pore that mercury enters is in the order of 3 nm. The relatively small throat size of pores in the Chang 7 and Chang 9 shales affected mercury porosity measurements (Fig. 15). Nevertheless, the covariation between the two sets of porosity values (Fig. 16c) is generally below 5%.

4. Discussion

Much greater pore volume of the two lowest-TOC samples and smaller pore volume of the two highest-TOC samples (Fig. 14c), as revealed by the N_2 adsorption measurements, suggest that mineral-associated pores dominated the pore systems of the samples in this study. This is related to the commonly observed presence of non-porous OM of various types with a large TOC range in the Yanchang shale (Fig. 5), as was also noted by Loucks et al. (2017). Also, clay minerals with well-developed intraparticle pores were identified in samples with a variety of TOC contents (Fig. 11a and b). These clay minerals seem to be poorly connected with the flow network in the shale since they were not infilled with solid bitumen (Fig. 11a), or only partially infilled to a small extent (Fig. 11b). It has been demonstrated by quantitative analysis of SEM images (Loucks et al., 2017; Wang et al., 2016) that intraparticle pores in clay platelets are the most important pore type in the Chang 7 and Chang 9 shales from the study area. The effects related to the pore development in the studied samples are discussed in detail below.

4.1. Preservation of primary pores within kerogen maceral

Round to oval pores have been identified in immature or mature woody fragments from the Tuscaloosa shale and Kimmeridge mudstones (Fishman et al., 2012; Lu et al., 2015), and they may be a result of the original cell structure. Löhr et al. (2015) suggested that the limited oil potential of woody OM may facilitate the preservation of primary pores in oil-mature woody OM in the Kimmeridge mudstones, because the primary migration of oil (could infill primary pores) may be a local process. However, this could not explain the more common occurrences of non-porous woody OM or type III kerogen in shales (Klaver et al., 2015; Löhr et al., 2015; Loucks et al., 2012, 2017; Pommer and Milliken, 2015), as shown in this study (Fig. 5). It was speculated that primary pores within woody OM could have been destroyed, since most of identified vitrinite and inertinite particles in this study are relatively small indicating a broken structure of original woody material. Moreover, the compaction effect on pore preservation could be plausible, as band-like woody OM extending more than 200 μm has been found in the Chang 7 shale (Loucks et al., 2017).

Most of the OM in sample C9-37 (medium TOC content: 4.65%, Table 1) was porous. Some OM in particular with a crosslinked nanofiber structure was observed to possess the best pore development in all types of OM in the studied samples (Fig. 8). Kerogen in the Barnett shale, Texas, with a porosity of 41% (VRo = 1.6%), has a sponge-like

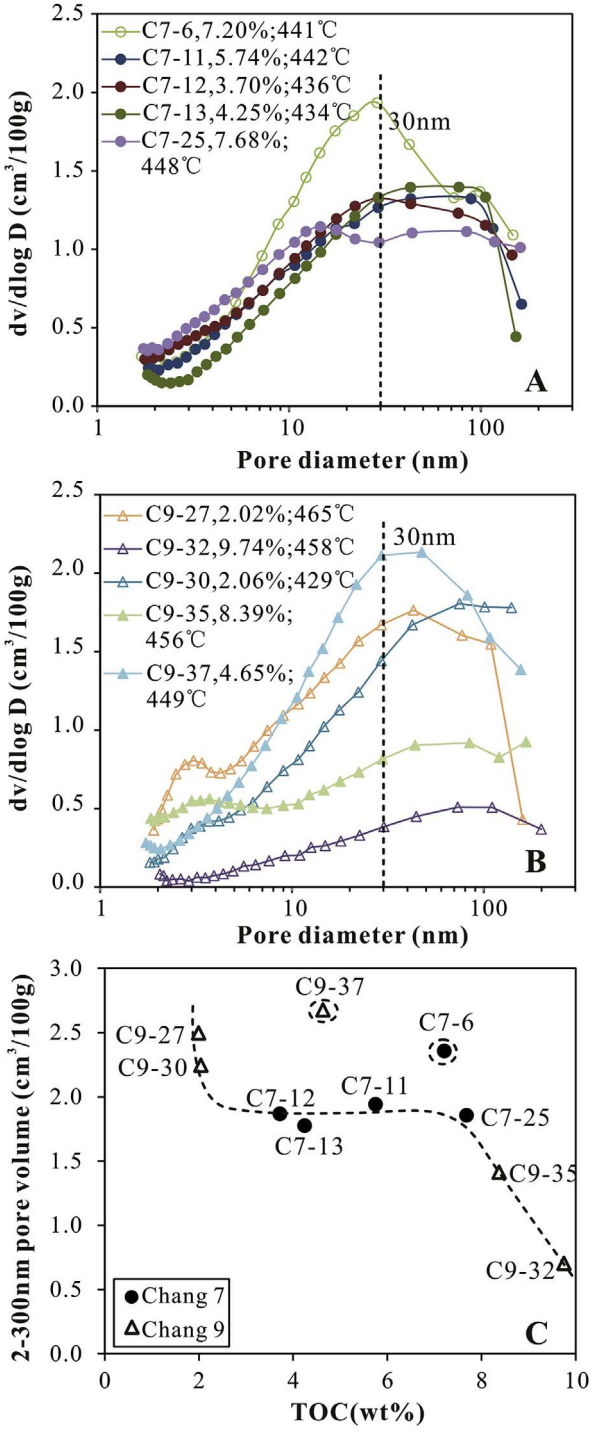

Fig. 14. (a), (b) Pore volume distribution vs. pore diameter derived from N_2 adsorption branches using the BJH model; (c) variation of TOC content vs. pore volume in the size range 2–300 nm, as measured by N_2 adsorption branches. In the legend, the TOC content and Tmax value are listed after sample name.

appearance at relatively low magnification (Loucks et al., 2012); when observed at high magnification, however, the pores are generally isolated or discrete, and tend to be equant (Loucks et al., 2012; Sondergeld et al., 2010). This differs totally from the appearance of the pores seen in sample C9-37 of the present study. Earlier, Loucks et al. (2009) had shown a high-porosity kerogen in the Barnett shale that indicated an obvious alignment of the pores, suggesting a primary internal structure. Klaver et al. (2015) presented a particle of solid bitumen containing abundant, relatively large pores of roughly round shape, indicating the

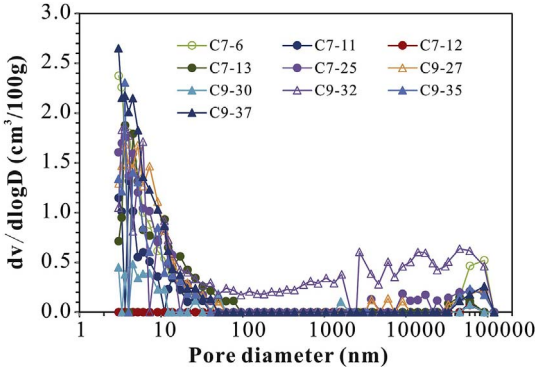

Fig. 15. Pore throat volume distribution of Chang 7 and Chang 9 shales, as determined by mercury intrusion.

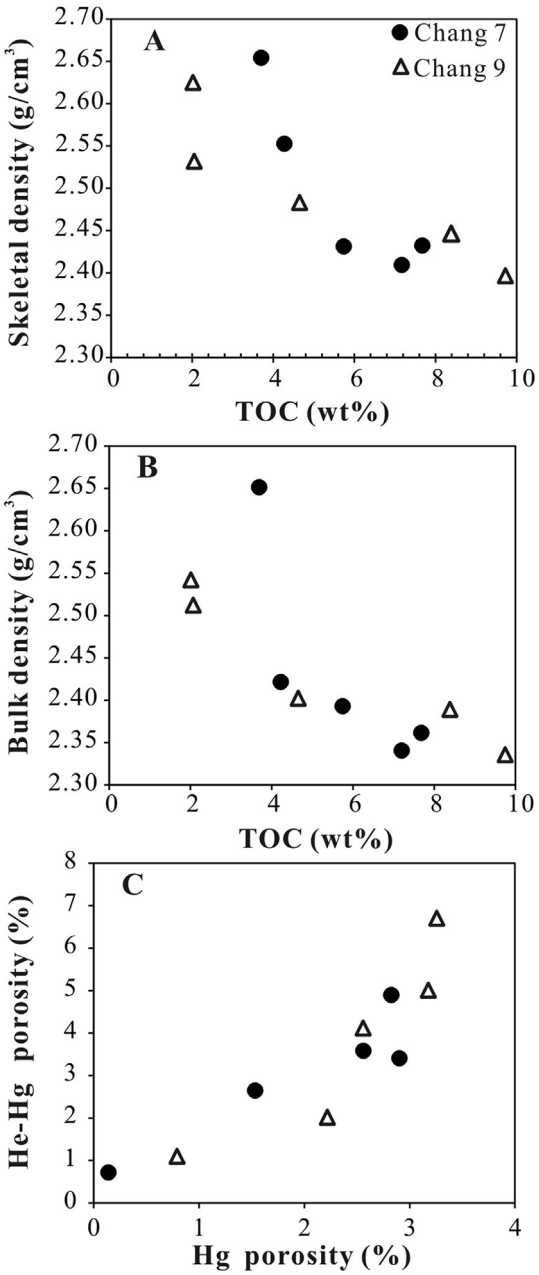

Fig. 16. Correlation between TOC and (a) skeletal density, and (b) bulk density; (c) relationship between porosity by Hg intrusion and He-Hg methods.

nucleation of gas or oil bubbles. One recent study reported the nanofiber structure in the Utica/Point Pleasant shales, Ohio (Alcantar-lopez, 2016), one of whose most notable features was the cross-linked network of organic fibers or bridges (Fig. 8a) that determine the size and shape of the pores; also the numerous pores within them were poorly aligned.

Alcantar-lopez (2016) demonstrated the progressive changes from sub-spherical units with increasing maturity to form a crosslinked network of OM for kerogen structures. Such changes, when associated with oil generation/swelling and subsequent oil expulsion/shrinkage, provide the routes for pore development during maturation. Alcantar-lopez (2016) further observed that a gel-like crosslinked kerogen structure forms as early as peak oil (VRo = 0.88%) and is clearly evident in shale with VRo > 1.1%. Tmax of sample C9-37 is ~450 °C and is located after the peak of the oil window in the crossplot of Tmax vs. S1/TOC ratio (Fig. 3b), which corresponds to the maturity range of samples with crosslinked organic nanofiber structure shown by Alcantar-lopez (2016). His study also pointed out that the OM was still characterized by the isolated, discrete spongy pores and complex pores when the samples were imaged on ion-milled surfaces using SEM. This is obviously different from the very porous OM in sample C9-37 (Fig. 8).

The very porous OM in sample C9-37 is probably derived from extracellular polymeric substances (EPS) composed of polysaccharides secreted by bacteria and microalgae (De Vuyst and Degeest, 1999), as shown by the SEM images of the fresh cleavage sample in Fig. 17. EPS have been observed to progressively form an alveolar network upon increasing bacterial stretching constraints in modern environments, and fossil alveolar networks have been preserved in subsequent lithification during diagenesis, producing a porous EPS (Pacton et al., 2007). In the photomicrograph of the ion-milled surface in which the possible EPS fossil was identified, abundant liptinites (colored yellow in fluorescent light, probably most are alginites or alginite fragments) were found (Fig. 17b). Unfortunately, it is still unclear whether any direct relationship existed between the possible EPS and the alginites because the EPS in the samples was too small to be identified with confidence using light microscopy. Abundant pores have been observed in fossil EPS in black shale and in bituminous laminae dating from the Cretaceous to the Miocene (Pacton et al., 2006, 2007, 2009; Ţabără et al., 2015). Porous EPS has also been found in modern lake sediments deposited in an alkaline hypersaline environment (Dupraz et al., 2004).

4.2. Pore development related to petroleum expulsion

Pores showing different degrees of development may have resulted from different petroleum expulsion processes (Loucks et al., 2009). Pores concentrated near the interface of OM and mineral grains (Fig. 6) may be related to the nucleation of gas bubbles on the surface of phyllosilicate minerals (Milliken et al., 2013; Pommer and Milliken, 2015). Experimental observation has shown that clay minerals preferentially catalyze the formation of gaseous hydrocarbons over other kinds (Tannenbaum and Kaplan, 1985), facilitating the nucleation and subsequent escape of gas bubbles on the mineral surfaces (Milliken et al., 2013). Although such pores were only found in small zones in the OM, they tended to interact when devolatilization or gas nucleation were significant (Fig. 6b and c). Shale samples in the Chang 7 and Chang 9 members were rich in clay minerals, most being mixed layered illite/smectite (Guo et al., 2014a). Clay minerals are recognized in shale by their straight or curved sheet-like shape. The OM in contact with clay minerals was porous (Fig. 6d and e); however, it was noticed that some OM in contact with clay minerals was non-porous, and some OM had pores in only small areas (Figs. 6d and e and 7b). This may occur when OM of different types remained close to each other, as was occasionally observed using light microscopy (Fig. 4i and j).

Isolated sponge-like pores (Fig. 7) might be related to the homogeneous nucleation of gas bubbles (Milliken et al., 2013); however, the relatively large discrete and complex pores showing some connectivity had been formed from the residual OM following oil expulsion, or by the interconnection of pores left by gas expulsion. Spongy and complex pores have been frequently found in the Yanchang shale (Fu et al., 2015; Ko et al., 2017; Lei et al., 2015; Loucks et al., 2017; Wang et al., 2015, 2016). Large bubble-shaped pores, generally several hundred nanometers in size (Fig. 10), may have been formed by the thermal cracking of bitumen into gas or oil, or by the release of entrapped water or petroleum in bitumen (Ko et al., 2017; Loucks et al., 2017). However, such pores observed in the studied samples could also have been formed during sample uploading and preparation, leading to the release of volatiles (Alcantar-lopez, 2016). Hence, whether these pores existed in situ is not yet clear. This explanation might also apply to the development of relatively large pores (300–400 nm, subrounded) coexisting with spongy pores (Fig. 7h).

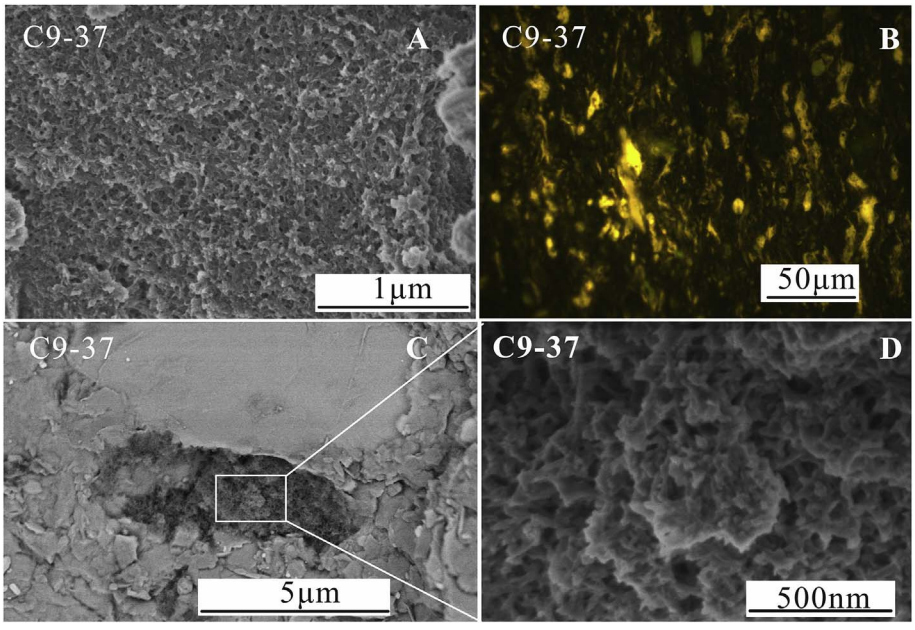

Fig. 17. (a, c, d) SEM images of fresh cleavage surface of sample C9-37 (TOC content 4.65 wt%) showing nanofiber structure pores in OM; (b) photomicrographs of the ion milled surface used for FE-SEM observation, took in fluorescent light using light microscopy.

4.3. Effect of residual bitumen on the pore development

A relatively large amount of bitumen (OM soluble in organic solvents) was left in the Chang 7 and Chang 9 shales (Fig. 3b, Table 1) after the generation and expulsion of petroleum. Migrating residual bitumen influenced the porosity by at least two processes: infilling mineral-associated interparticle pores, and also by blocking OM pores; this is one of the major reasons for significantly lowered shale porosity, based on the evidence from studies of both naturally occurred and thermally simulated samples (Guo et al., 2017; Löhr et al., 2015; Loucks et al., 2009, Loucks and Reed, 2014; Mastalerz et al., 2013; Pommer and Milliken, 2015). Several recent studies comparing low-pressure gas adsorption before and after the solvent extraction of shales within the oil window have shown significant enlargement of pore volume after solvent extraction (Valenza et al., 2013; Wei et al., 2014; Zargari et al., 2015). Similar work has also been reported for the Chang 7 and Chang 9 shales from the Ordos Basin (Guo et al., 2014a,b; Li et al., 2016; Liu et al., 2016; Xiong et al., 2016). These studies have shown that the surface area and N_2 adsorption capacity of samples increased after solvent extraction. The increment is more significant for samples with higher TOC content, and good positive correlation between surface area and TOC content could be established for extracted samples (Liu et al., 2016). However, for un-extracted samples, there is a negative relationship between surface area and TOC content. Therefore, increased pore surface area could be related to the mineral and OM associated pores. SEM imaging has shown that pores in OM which were invisible before extraction re-emerged after extraction (Löhr et al., 2015). Mineral pores that had been vacant before oil generation were occupied by migrating residual bitumen along the mineral margin, leaving open pores in the center at the oil generation stage (Ko et al., 2016). Mineral-associated pores were most clearly observed in sample C9-27 (Fig. 10), demonstrating that mineral pores could be occupied by residual bitumen during thermal maturation. In most cases, mineral pores and fractures were completely occupied by solid bitumen (which may have been the solid residue after secondary cracking of soluble bitumen, Fig. 5d and e).

Besides infilling, occupation of the surface of solid OM by soluble bitumen prevents the adsorption of gases on the pores, reducing the amount of adsorbed gas in low-pressure gas adsorption analysis. In addition, adsorption of soluble bitumen by solid OM such as kerogen would result in the swelling of solid OM and appearing to behave like organic macromolecules (Ertas et al., 2006; Kelemen et al., 2006; Pepper and Corvi, 1995; Ritter, 2003; Sandvik et al., 1992). It has been suggested that the adsorption of residual bitumen and resultant swelling of structural units of solid OM in shale is one of the important factors in reducing the OM porosity related to the space within a connected OM framework (Alcantar-lopez, 2016). One such typical solid OM coated with a fluid organic film through the open pore inside solid bitumen was observed in an SEM image of a Chang 7 shale sample (Fig. 18). This is very similar to the solid OM illustrated for the Eagle Ford shale (Fig. 10 in Alcantar-lopez, 2016). He also showed the nanoparticle structure and cross-linked network of nanofibers of solid OM (possibly kerogen or solid bitumen) after CO_2-toluene cleaning of shale samples within the oil window.

Both Chang 7 and Chang 9 shales generally contain more soluble bitumen with higher TOC content (Guo et al., 2014a). Therefore, the influence of residual bitumen on the shale porosity was more intense in samples with relatively high content (Liu et al., 2016), which is possibly responsible for the relatively lower pore volume of the two samples with relatively high TOC content (Fig. 14c). However, sample C9-32, with the highest TOC content, showed little increase of pore volume after solvent extraction (2–300 nm, measured by N_2 adsorption isotherms, Guo et al., 2014b). By contrast, micropore volume determined by CO_2 adsorption analysis showed a large increment following solvent extraction. Therefore, it is evident that bitumen infilling and adsorption are not the key factors resulting in both low meso–macro pore volume (2–300 nm, Guo et al., 2014b) and the complete lack of visible pores in SEM images (greater than 5 nm, Fig. 5f), but bitumen infilling and adsorption greatly lowered the micropore volume in sample C9-32.

4.4. Effect of compaction on pore development

Compaction is one of the main causes of reduction in shale porosity during diagenesis and catagenesis (Ko et al., 2017; Loucks and Reed, 2014; Mastalerz et al., 2013; Pommer and Milliken, 2015). The increase in the porosity of shales has been shown to peak and even decrease with increasing TOC content beyond a certain level (Milliken et al., 2013; Zeng et al., 2016). This is probably related to the greater influence of compaction on the porosity of shale with more abundant OM due to the more ductile framework in the shale. As stated in section 4.3, the very low pore volume of pores with diameters of 2–300 nm and lack of visible pores in sample C9-32 with the highest TOC content (Figs. 5f and 14b, c) was not related to the bitumen infilling and adsorption effect, but is attributable to the effect of high compaction on pore development. This implies that relatively large pores of both primary and secondary origin have been destroyed and/or altered into micropores, since the CO_2 adsorption analysis of this sample has shown more than three times the micropore volume in the other samples in Fig. 12 and Table 1. Löhr et al. (2015) reported that no pores were visible in amorphous OM in immature Woodford shale (Oklahoma), particularly when aggregated with clay minerals. Therefore, the effect of high compaction could be related to the laminar structure of OM–mineral aggregates (e.g., clays with other minor minerals: Fig. 5f) in addition to the relatively high TOC content. Such laminar structures are particularly susceptible to the effects of compaction, which would then reduce the number of intraparticle pores within the minerals (Fishman et al., 2012).

The OM in the photomicrographs and SEM images varied in size from a few micrometers to hundreds of micrometers (Figs. 5–8). Although the pores in porous OM differed greatly in size and shape, they generally appeared within small OM grains (Figs. 7 and 8). Such OM was from a few hundreds of nanometers to several micrometers long, which possibly prevented pores within the OM from being greatly influenced by compaction. Chang 7 shale was reported to be greatly

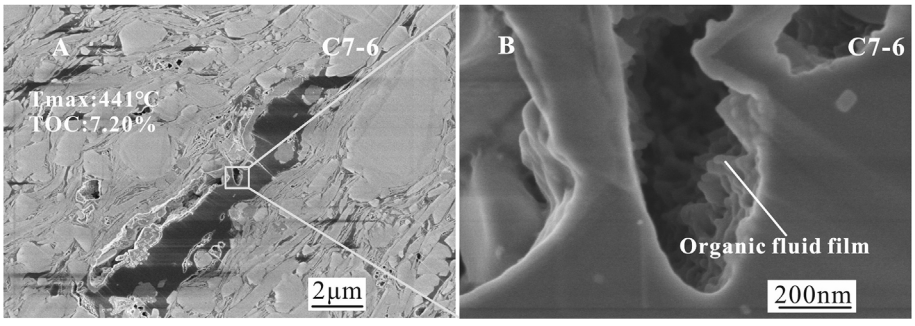

Fig. 18. (a) Solid bitumen showing relatively large open pores in sample C7-6. The pores may be a result of oil expulsion during sample uploading and preparation. (b) Film of organic fluid coating solid OM observed in the pores shown in panel a.

affected by compaction due to a lack of early cementation, which resulted in relatively small spongy pores in the shale (Ko et al., 2017). Very abundant pores within the probable EPS fossils observed in sample C9-37 (Fig. 8) ranged from 10 to 250 nm in size; however, previously reported images of rock surfaces indicate that the pores in typical fossil EPS (Pacton et al., 2006, 2007, 2009; Ţabără et al., 2015) generally varied from 100 nm to several micrometers. These rocks are mostly immature, as suggested by their very low Tmax (Pacton et al., 2009). Therefore, organic pores in sample C9-37 may have been greatly altered and had thus become relatively small, although a thermal alteration effect on the pores cannot be fully excluded.

4.5. Pore development with thermal maturity

The pore evolution with progressive thermal maturity has been among the most widely discussed topics in the petroleum industry over the past ten years (Jarvie et al., 2007; Mastalerz et al., 2013; Pommer and Milliken, 2015; Curtis et al., 2012). It had earlier been supposed that pore development is a result of carbon loss, and that volume changes arose as a result of petroleum generation and expulsion from kerogen (Jarvie et al., 2007). Shortly afterwards, SEM observations combined with ion beam milling showed that nanometer-scale pores are often visible in relatively highly matured shale samples, which demonstrated the relationship between OM maturation and pore development (Loucks et al., 2009; Wang and Reed, 2009). Solid bitumen in shale, formed by the secondary cracking of bitumen that had either migrated or that was coexisting (by adsorption or solution) with residual kerogen, is one of the most common OM types in which spongy and complex pores have been observed (Bernard et al., 2012). This also supported the suggestion that pore development was facilitated by OM transformation. Key factors and processes controlling pore evolution during the whole maturation process have been proposed, based either on studies of relatively large natural sample sets (Loucks and Reed, 2014; Löhr et al., 2015; Mastalerz et al., 2013; Pommer and Milliken, 2015), or on thermal simulation of a single sample (Chen and Xiao, 2014; Guo et al., 2017; Ko et al., 2016; Sun et al., 2015; Tang et al., 2015). These studies elucidated the complicated evolutionary trends of pore development relating to the maturity of shale, since pore development is not only related to OM transformation but also to compaction and mineral composition. In addition, OM transformation takes place as a result of several types of chemical and physical processes, each of which is influenced by the abundance, type and composition of the OM. Therefore, progressive incremental shale porosity may not be evident with elevated maturities, even in the same shale unit (Curtis et al., 2012; Milliken et al., 2013).

The relationship between maturity and pore volume has been shown for the Chang 7 shale from the southeastern Ordos Basin (Fu et al., 2015; Jiang et al., 2016); however, this was not supported in a more recent study (Ko et al., 2017). The sample selection in the present study carefully considered the variation in maturity, as shown by Rock-Eval analytical results in Fig. 3. The 10 samples showed no clear trend for pore volume (0.35–300 nm) or bulk porosity with increasing Tmax (Fig. 19). The relatively small sample set could be one factor influencing determination of the maturity trend of the porosity. For pore volumes ranging from 0.35 to 300 nm, the two samples with the highest TOC content (C9-32 and C9-35) deviated significantly from the other eight samples (Fig. 19a). If these two samples were excluded from the statistics, a weak positive correlation of pore volume and total porosity with Tmax is observed (Fig. 19). In sections 4.3 and 4.4, the very low level of pore development in sample C9-32 is demonstrated to be mainly related to compaction rather than bitumen infilling or adsorption. These results thus suggest that although maturity has affected pore development in shale to some extent, compaction has possibly had greater impact on pore development in the studied samples. Mineral-associated pores were the dominant pore type in most of the studied samples (Fig. 14c); however, samples C9-37 and C7-6 were exceptions, since both samples contained relatively abundant porous OM (Figs. 7 and 8). Different pore types may exhibit different evolutionary trends with increasing maturity, and could also be affected by compaction at distinct levels. Therefore, determining the relationship between shale porosity and maturity should be performed on the basis of a careful evaluation of other important factors such as pore type, compaction effect, etc.

5. Conclusion

SEM observation, combined with low-pressure gas adsorption and mercury intrusion, was used to study the distribution and controlling factors of pores in the lacustrine Yanchang shale within the oil window. The results support current views on the pore characteristics of the shale:

(1) The shale in the Chang 7 and Chang 9 members generally had relatively low total porosities and poor connectivity between pores.
(2) Abundant OM displaying spongy and complex pore texture was observed in some of studied samples. This was supported by pore-volume distribution measurements by N_2 adsorption analysis.
(3) Most of the pore types reported for marine shale also appeared in the lacustrine Chang 7 and Chang 9 shales; for example: OM pores lining OM-mineral boundaries as a result of gas nucleation; devolatilization microfractures within the OM; superior pore development in OM possessing a nanofiber network; intraparticle pores related to mineral dissolution; and relatively large intraparticle pores in clay platelets.

This study has also provided some pointers to improve the understanding of pore development in lacustrine shale, however, caution should be taken when extrapolating the results across the basin considering that only ten samples were investigated.

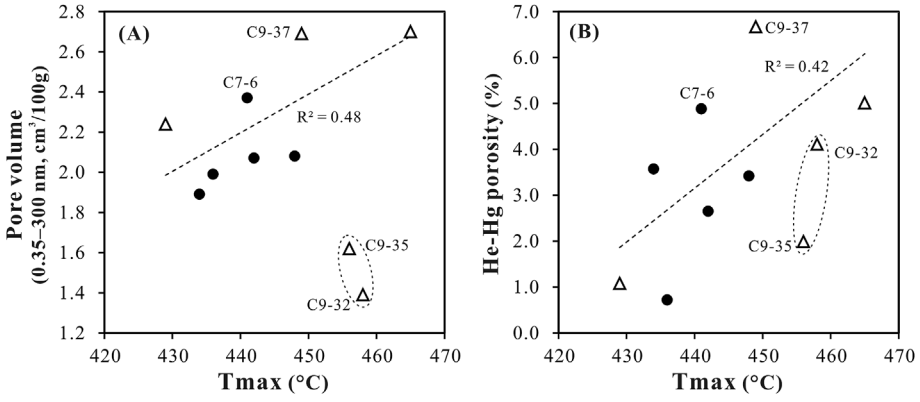

Fig. 19. Relationships between Tmax and (a) total pore volume (0.3–300 nm); and (b) total He–Hg porosity. Dashed lines show linear regression results of all studied samples except two samples (C9-32 and C9-35). Filled cycles and blank triangles indicate Chang 7 shale and Chang 9 shale, respectively.

(1) Pores were better developed in OM of several hundreds of nanometers to several micrometers in size, which is mainly related to different petroleum expulsion processes and compaction effect. Among the porous OM types are probably EPS having an alveolar structure, which have been affected by compaction and maturation, leading to a substantial reduction in pore size. Abundant alginites were commonly identified in shale with this type of OM.
(2) The ultra-low volume of pores larger than 2 nm in the highest TOC-content sample, as indicated by N_2 adsorption, was attributed to the dominance of organic laminae without visible pores; however, CO_2 adsorption indicated that the sample possessed a much greater micropore volume than others. Meso- and macropores in the samples were not noticeably affected by bitumen infilling, but probably did not develop due to a significant compaction effect on primary and/or secondary OM pores.
(3) No visible pores were present in a variety of OM types (woody relics, migrated solid bitumen, and OM laminae interbedded with clay minerals). The OM varied greatly in both size and shape.
(4) Small microfractures, generally shorter than 2 μm, were possibly formed by the connection of massive spongy pores developed within OM.

Acknowledgements

This work was supported by funds from the Strategic Priority Research Program (grant number XDB10010201), Natural Science Foundation of China (grant number 41621062), Shaanxi Science & Technology Co-ordination & Innovation Project (grant number 2012KTZB03-03-01-01). The authors appreciate the technical assistance of Prof. Dehan Liu, Dr. Qin Zhou, Dr. Jia Xia in the microscopic observation, FE-SEM observation, MIP analysis. We appreciate Dr. Xuan Tang and five anonymous reviewers very much for valuable comments and suggestions that have greatly improved the manuscript. Dr. Barry J. Katz is acknowledged for great patience of handling and editing the manuscript and for many constructive suggestions.

References

Alcantar-lopez, L., 2016. Understanding organic matter structural changes with increasing thermal maturity from oil shale plays through SEM imaging. In: Unconventional Resources Technology Conference, URTeC control ID number 2456170.
Barret, E.P., Joyner, L.G., Halenda, P.P., 1951. The determination of pore volume and area distribution in porous substances. I. Computations from nitrogen isotherms. J. Am. Chem. Soc. 73, 373–380.
Bernard, S., Wirth, R., Schreiber, A., Schulz, H.M., Horsfield, B., 2012. Formation of nanoporous pyrobitumen residues during maturation of the Barnett shale (Fort Worth Basin). Int. J. Coal Geol. 103, 3–11.
Bustin, A.M.M., Bustin, R.M., Cui, X., 2008. Importance of fabric on the production of gas shales. In: SPE Unconventional Reservoirs Conference, Keystone, pp. 29 10–12 February, 2008. SPE Paper 114167.
Chalmers, G.R., Bustin, R.M., Power, I.M., 2012. Characterization of gas shale pore systems by porosimetry, pycnometry, surface area, and field emission scanning electron microscopy/transmission electron microscopy image analyses: examples from the Barnett, Woodford, Haynesville, Marcellus, and Doig units. AAPG Bull. 96, 1099–1119.
Chen, J., Xiao, X., 2014. Evolution of nanoporosity in organic-rich shales during thermal maturation. Fuel 129, 173–181.
Curtis, M.E., Cardott, B.J., Sondergeld, C.H., Rai, C.S., 2012. Development of organic porosity in the Woodford Shale with increasing thermal maturity. Int. J. Coal Geol. 103, 26–31.
De Vuyst, L., Degeest, B., 1999. Heteropolysaccharides from lactic acid bacteria. FEMS (Fed. Eur. Microbiol. Soc.) Microbiol. Rev. 23, 153–177.
Dupraz, C., Visscher, P.T., Baumgartner, L.K., Reid, R.P., 2004. Microbe-mineral interactions: early carbonate precipitation in a hypersaline lake (Eleuthera Island, Bahamas). Sedimentology 51, 745–765.
Ertas, D., And, S.R.K., Halsey, T.C., 2006. Petroleum expulsion Part 1. Theory of kerogen swelling in multicomponent solvents. Energy Fuels 20, 295–300.
Fang, C.L., Amro, M., Jiang, G.S., Lu, H.Z., 2016. Laboratory studies of non-marine shale porosity characterization. J. Nat. Gas Sci. Eng. 33, 1181–1189.
Fishman, N.S., Hackley, P.C., Lowers, H.A., Hill, R.J., Egenhoff, S.O., Eberl, D.D., Blum, A.E., 2012. The nature of porosity in organic-rich mudstones of the Upper Jurassic Kimmeridge Clay Formation, North Sea, offshore United Kingdom. Int. J. Coal Geol. 103, 32–50.
Fu, H.J., Wang, X.Z., Zhang, L.X., Gao, R.M., Li, Z.T., Xu, T., Zhu, X.L., Xu, W., Li, Q., 2015. Investigation of the factors that control the development of pore structure in lacustrine shale: a case study of block X in the Ordos Basin, China. J. Nat. Gas Sci. Eng. 26, 1422–1432.
Gan, H., Nandi Jr., S.P., P.L.W, 1972. Nature of the porosity in American coals. Fuel 51, 272–277.
Gregg, S.J., Sing, K.S.W., 1982. Adsorption, Surface Area and Porosity, second ed. Academic Press, London.
Guo, H.J., Jia, W.L., Peng, P.A., Lei, Y.H., Luo, X.R., Cheng, M., Wang, X.Z., Zhang, L.X., Jiang, C.F., 2014a. The composition and its impact on the methane sorption of lacustrine shales from the Upper Triassic Yanchang Formation, Ordos Basin, China. Mar. Petrol. Geol. 57, 509–520.
Guo, H.J., Wang, X.Z., Zhang, L.X., Jiang, C.F., Jia, W.L., Peng, P.A., Lei, Y.H., Luo, X.R., Cheng, M., 2014b. Adsorption of N_2 and CO_2 on mature shales before and after extraction and its implication for investigations of pore structures. Geochimica 43, 408–414 (in Chinese with English abstract).
Guo, H.J., Jia, W.L., Peng, P.A., Zeng, J., He, R.L., 2017. Evolution of organic matter and nanometer-scale pores in an artificially matured shale undergoing two distinct types of pyrolysis: a study of the Yanchang Shale with type II kerogen. Org. Geochem. 105, 56–66.
Hackley, P.C., Cardott, B.J., 2016. Application of organic petrography in North American shale petroleum systems: a review. Int. J. Coal Geol. 163, 8–51.
Hackley, P.C., Zhang, L.X., Zhang, T.W., 2017. Organic petrology of peak oil maturity Triassic Yanchang Formation lacustrine mudrocks, Ordos Basin, China. Interpretation 5, SF211–SF223.
Jarvie, D.M., Hill, R.J., Ruble, T.E., Pollastro, R.M., 2007. Unconventional shale-gas systems: the Mississippian Barnett Shale of north-central Texas as one model for thermogenic shale-gas assessment. AAPG Bull. 91, 475–499.
Ji, L.M., Xu, J.L., 2007. Triassic acritarchs and its relation to hydrocarbon source rock in Ordos Basin. Acta Pet. Sin. 28, 40–43 48 (in Chinese with English abstract).
Ji, L.M., Wang, S.F., Xu, J.L., 2006. Acritarch assemblage in Yanchang Formation in eastern Gansu province and its environmental implications. Earth Sci. J. China Univ. Geosci. 31, 798–806 (in Chinese with English abstract).
Ji, L.M., Li, J.F., Song, Z.G., 2009. Petroleum geological significance of Botryococcus in Triassic Yanchang Formation, Ordos Basin. Petrol. Explor. Dev. 36, 156–165 (in Chinese with English abstract).
Jiang, F.J., Chen, D., Wang, Z.F., Xu, Z.Y., Chen, J., Liu, L., Huyan, Y.Y., Liu, Y., 2016. Pore characteristic analysis of a lacustrine shale: a case study in the Ordos Basin, NW China. Mar. Petrol. Geol. 73, 554–571.
Katz, B.J., 1990. Controls on distribution of lacustrine source rocks through time and space. In: In: Katz, B.J. (Ed.), Lacustrine Basin Evolution—case Studies and Modern Analogs, vol. 50. AAPG (Tulsa) Mem, pp. 61–76.
Katz, B., Lin, F., 2014. Lacustrine basin unconventional resource plays: key differences. Mar. Petrol. Geol. 56, 255–265.
Kelemen, S., Walters, C., Ertas, D., Kwiatek, L., Curry, D., 2006. Petroleum expulsion Part 2. Organic matter type and maturity effects on kerogen swelling by solvents and thermodynamic parameters for kerogen from regular solution theory. Energy Fuels 20, 301–308.
Klaver, J., Desbois, G., Littke, R., Urai, J.L., 2015. BIB-SEM characterization of pore space morphology and distribution in postmature to overmature samples from the Haynesville and Bossier Shales. Mar. Petrol. Geol. 59, 451–466.
Ko, L.T., Loucks, R.G., Zhang, T., Ruppel, S.C., Shao, D., 2016. Pore and pore network evolution of Upper Cretaceous Boquillas (Eagle Ford–equivalent) mudrocks: results from gold tube pyrolysis experiments. AAPG Bull. 100, 1693–1722.
Ko, L.T., Loucks, R.G., Ruppel, Milliken, K.L., Liang, Q.S., Zhang, T.W., Sun, X., Hackley, P.C., Ruppel, S., Peng, S., 2017. Controls on pore types and pore-size distribution in the Upper Triassic Yanchang Formation, Ordos Basin, China: implications for pore-evolution models of lacustrine mudrocks. Interpretation 5, SF127–SF148.
Kuila, U., Prasad, M., 2013. Specific surface area and pore-size distribution in clays and shales. Geophys. Prospect. 61, 341–362.
Kuila, U., McCarty, D.K., Derkowski, A., Fischer, T.B., Topór, T., Prasad, M., 2014. Nano-scale texture and porosity of organic matter and clay minerals in organic-rich mudrocks. Fuel 135, 359–373.
Lei, Y.H., Luo, X.R., Wang, X.Z., Zhang, L.X., Jiang, C.F., Yang, W., Yu, Y.X., Cheng, M., Zhang, L.K., 2015. Characteristics of silty laminae in Zhangjiatan Shale of southeastern Ordos Basin, China: implications for shale gas formation. AAPG Bull. 99, 661–687.
Li, J., Zhou, S.X., Li, Y.J., Ma, Y., Yang, Y.N., Li, C.C., 2016. Effect of organic matter on pore structure of mature lacustrine organic-rich shale: a case study of the Triassic Yanchang shale, Ordos Basin, China. Fuel 185, 421–431.
Liu, G.H., Huang, Z.L., Jiang, Z.X., Chen, J.F., Chen, F.R., Xing, J.Y., 2016. Gas adsorption capacity calculation limitation due to methane adsorption in low thermal maturity shale: a case study from the Yanchang Formation, Ordos Basin. J. Nat. Gas Sci. Eng. 30, 106–118.
Löhr, S.C., Baruch, E.T., Hall, P.A., Kennedy, M.J., 2015. Is organic pore development in gas shales influenced by the primary porosity and structure of thermally immature organic matter? Org. Geochem. 87, 119–132.
Loucks, R.G., Reed, R.M., 2014. Scanning-electron-microscope petrographic evidence for distinguishing organic matter pores associated with depositional organic matter versus migrated organic matter in mudrocks. Gulf Coast Assoc. Geol. Soc. 3, 51–60.
Loucks, R.G., Reed, R.M., 2016. Natural microfractures in unconventional shale-oil and shale-gas systems: real, hypothetical, or wrongly defined. GCAGS J. 5, 64–72.
Loucks, R.G., Reed, R.M., Ruppel, S.C., Jarvie, D.M., 2009. Morphology, genesis, and distribution of nanometer-scale pores in siliceous mudstones of the Mississippian Barnett shale. J. Sediment. Res. 79, 848–861.
Loucks, R.G., Reed, R.M., Ruppel, S.C., Hammes, U., 2012. Spectrum of pore types and

networks in mudrocks and a descriptive classification for matrix-related mudrock pores. AAPG Bull. 96, 1071–1098.
Loucks, R.G., Ruppel, S.C., Wang, X.Z., Ko, L., Peng, S., Zhang, T.W., Rowe, H.D., Smith, P., 2017. Pore types, pore-network analysis, and pore quantification of the lacustrine shale-hydrocarbon system in the Late Triassic Yanchang Formation in the southeastern Ordos Basin, China. Interpretation 5, SF63–SF79.
Lu, J.M., Ruppel, S.C., Rowe, H.D., 2015. Organic matter pores and oil generation in the Tuscaloosa marine shale. AAPG Bull. 99, 333–357.
Mastalerz, M., Schimmelmann, A., Drobniak, A., Chen, Y., 2013. Porosity of Devonian and Mississippian New Albany Shale across a maturation gradient: insights from organic petrology, gas adsorption, and mercury intrusion. AAPG Bull. 97, 1621–1643.
Milliken, K.L., Rudnicki, M., Awwiller, D.N., Zhang, T.W., 2013. Organic matter-hosted pore system, Marcellus Formation (Devonian), Pennsylvania. AAPG Bull. 97, 177–200.
Milliken, K.L., Shen, Y., Ko, L.T., Liang, Q.S., 2017. Grain composition and diagenesis of organic-rich lacustrine tarls, Triassic Yanchang Formation, Ordos Basin, China. Interpretation 5, SF189–SF210.
Pacton, M., Fiet, N., Gorin, G., 2006. Revisiting amorphous organic matter in Kimmeridgian laminites: what is the role of the vulcanization process in the amorphization of organic matter? Terra. Nova 18, 380–387.
Pacton, M., Fiet, N., Gorin, G.E., 2007. Bacterial activity and preservation of sedimentary organic matter: the role of exopolymeric substances. Geomicrobiol. J. 24, 571–581.
Pacton, M., Gorin, G., Fiet, N., 2009. Occurrence of photosynthetic microbial mats in a Lower Cretaceous black shale (central Italy): a shallow-water deposit. Facies 55, 401–419.
Pepper, A.S., Corvi, P.J., 1995. Simple Kinetic-models of petroleum formation. 3. Modleing an open system. Mar. Petrol. Geol. 12, 417–452.
Pommer, M., Milliken, K., 2015. Pore types and pore-size distributions across thermal maturity, Eagle Ford Formation, southern Texas. AAPG Bull. 99, 1713–1744.
Ritter, U., 2003. Solubility of petroleum compounds in kerogen: implications for petroleum expulsion. Org. Geochem. 34, 319–326.
Ross, D.J.K., Bustin, R.M., 2007. Shale gas potential of the Lower Jurassic Gordondale Member, northeastern British Columbia, Canada. Bull. Can. Petrol. Geol. 55, 51–75.
Ross, D.J.K., Bustin, R.M., 2009. The importance of shale composition and pore structure upon gas storage potential of shale gas reservoirs. Mar. Petrol. Geol. 26, 916–927.
Ruppel, S.C., Rowe, H., Milliken, K., Gao, C., Wan, Y.P., 2017. Facies, rock attributes, stratigraphy, and depositional environments: Yanchang Formation, central Ordos Basin, China. Interpretation 5, SF15–SF29.
Sandvik, E., Young, W., Curry, D., 1992. Expulsion from hydrocarbon sources: the role of organic absorption. Org. Geochem. 19, 77–87.
Schieber, J., 2010. Common themes in the formation and preservation of intrinsic porosity in shales and mudstones-illustrated with examples across the Phanerozoic. In: SPE Unconventional Gas Conference, SPE paper 132379.
Sing, K.S.W., 1985. Reporting physisorption data for gas/solid systems with special reference to the determination of surface area and porosity (Recommendations 1984). Pure Appl. Chem. 57, 603–619.
Slatt, R.M., O'Brien, N.R., 2011. Pore types in the Barnett and Woodford gas shales: contribution to understanding gas storage and migration pathways in fine-grained rocks. AAPG Bull. 95, 2017–2030.
Sondergeld, C.H., Ambrose, R.J., Rai, C.S., Moncrieff, J., 2010. Micro-structural studies of gas shales. In: SPE Unconventional Gas Conference, SPE paper 131771.
Sun, L., Tuo, J., Zhang, M., Wu, C., Wang, Z., Zheng, Y., 2015. Formation and development of the pore structure in Chang 7 member oil-shale from Ordos Basin during organic matter evolution induced by hydrous pyrolysis. Fuel 158, 549–557.
Tang, X., Zhang, J.C., Wang, X.Z., Yu, B.S., Ding, W.L., Xiong, J.Y., Yang, Y.T., Wang, L., Yang, C., 2014. Shale characteristics in the southeastern Ordos Basin, China: implications for hydrocarbon accumulation conditions and the potential of continental shales. Int. J. Coal Geol. 128, 32–46.
Tang, X., Zhang, J., Jin, Z., Xiong, J., Lin, L., Yu, Y., Han, S., 2015. Experimental investigation of thermal maturation on shale reservoir properties from hydrous pyrolysis of Chang 7 shale, Ordos Basin. Mar. Petrol. Geol. 64, 165–172.
Tannenbaum, E., Kaplan, I.R., 1985. Role of minerals in the thermal alteration of organic-matter-I: generation of gases and condensates under dry condition. Geochem. Cosmochim. Acta 49, 2589–2604.
Tian, H., Pan, L., Xiao, X., Wilkins, R.W.T., Meng, Z., Huang, B., 2013. A preliminary study on the pore characterization of Lower Silurian black shales in the Chuandong Thrust Fold Belt, southwestern China using low pressure N_2, adsorption and FE-SEM methods. Mar. Petrol. Geol. 48, 8–19.
Valenza II, J.J., Drenzek, N., Marques, F., Pagels, M., Mastalerz, M., 2013. Geochemical controls on shale microstructure. Geology 41, 611–614.
Wang, F.P., Reed, R.M., 2009. Pore networks and fluid flow in gas shales. In: SPE Annual Technical Conference and Exhibition, SPE 124253.
Wang, X.Z., Gao, S.L., Gao, C., 2014. Geological features of Mesozoic continental shale gas in south of Ordos Basin, NW China. Petrol. Explor. Dev. 41, 294–304 (in Chinese with English abstract).
Wang, Y., Zhu, Y.M., Wang, H.Y., Feng, G.J., 2015. Nanoscale pore morphology and distribution of lacustrine shale reservoirs: examples from the Upper Triassic Yanchang Formation, Ordos Basin. J. Energy Chem. 24, 512–519.
Wang, X.Z., Zhang, L.X., Li, Z.T., Fu, H.J., 2016. Pore type classification scheme for continental Yanchang shale in Ordos Basin and its geological significance. Oil Gas Geol. 37, 1–7 (in Chinese with English abstract).
Washburn, E.W., 1921. Note on the method of determining the distribution of pore sizes in a porous material. Proc. Natl. Acad. Sci. Unit. States Am. 7, 115–116.
Wei, L., Mastalerz, M., Schimmelmann, A., Chen, Y., 2014. Influence of Soxhlet-extractable bitumen and oil on porosity in thermally maturing organic-rich shales. Int. J. Coal Geol. 132, 38–50.
Xiong, F.Y., Jiang, Z.X., Chen, J.F., Wang, X.Z., Huang, Z.L., Liu, G.H., Chen, F.R., Li, Y.R., Chen, L., Zhang, L.X., 2016. The role of the residual bitumen in the gas storage capacity of mature lacustrine shale: a case study of the Triassic Yanchang shale, Ordos Basin, China. Mar. Petrol. Geol. 69, 205–215.
Yang, H., Li, S.X., Liu, X.Y., 2013. Characteristics and resource prospects of tight oil and shale oil in Ordos Basin. Acta Pet. Sin. 34, 1–11 (in Chinese with English abstract).
Yang, H., Niu, X.B., Xu, L.M., Feng, S.B., You, Y., Liang, X.W., Wang, F., Zhang, D.D., 2016. Exploration potential of shale oil in Chang7 Member, Upper Triassic Yanchang Formation, Ordos Basin, NW China. Petrol. Explor. Dev. 43, 511–520 (in Chinese with English abstract).
Zargari, S., Canter, K.L., Prasad, M., 2015. Porosity evolution in oil-prone source rocks. Fuel 153, 110–117.
Zeng, J., Jia, W.L., Peng, P.A., Guan, C.G., Zhou, C.M., Yuan, X.L., Chen, S.S., Yu, C.L., 2016. Composition and pore characteristics of black shales from the Ediacaran Lantian Formation in the Yangtze Block, south China. Mar. Petrol. Geol. 76, 246–261.
Zhang, W.Z., Yang, H., Fu, S.T., Zan, C.L., 2007. On the development mechanism of the lacustrine high-grade hydrocarbon source rocks of Chang 9(1) Member in Ordos Basin. Sci. China Earth Sci. 50, 39–46.
Zhang, M.Z., Ji, L.M., Wu, Y.D., He, C., 2015a. Palynofacies and geochemical analysis of the Triassic Yanchang Formation, Ordos Basin: implications for hydrocarbon generation potential and the paleoenvironment of continental source rocks. Int. J. Coal Geol. 152, 159–176.
Zhang, W.Z., Yang, H., Yang, W.W., Wu, K., Liu, F., 2015b. Assessment of geological characteristics of lacustrine shale oil reservoir in Chang7 Member of Yanchang Formation, Ordos Basin. Geochimica 44, 505–515 (in Chinese with English abstract).
Ţabără, D., Pacton, M., Makou, M., Chirila, G., 2015. Palynofacies and geochemical analysis of oligo-miocene bituminous rocks from the Moldavidian Domain (eastern Carpathians, Romania): implications for petroleum exploration. Rev. Palaeobot. Palynol. 216, 101–122.